Cracking of quasi-brittle structures under monotonic and cyclic loadings: a d^+/d^- damage model with stiffness recovery in shear

Miguel Cervera[1], Claudia Tesei[2]*, Giulio Ventura[3]

[1]International Center for Numerical Methods in Engineering, Universidad Politécnica de Cataluña; e-mail: miguel.cervera@upc.edu

[2, 3] Department of Structural, Building and Geotechnical Engineering, Politecnico di Torino e-mail: claudia.tesei@polito.it; giulio.ventura@polito.it

* Correspondence: claudia.tesei@polito.it; Tel.: + 39 011 0904849.

Abstract

In the present paper, a new d^+/d^- damage model apt for quasi-brittle materials is described and its validation is carried out considering unreinforced concrete, reinforced concrete and masonry elements.

Two independent scalar damage variables, d^+ and d^-, in combination with the split of the reversible strain tensor into its positive and negative counterparts, are adopted in order to simulate the pronounced dissimilar response under tension and compression, typical of these materials. An energy-equivalent framework is considered for representing the orthotropy induced in the material by the degradation process, with the consequence that a thermodynamically consistent constitutive operator, positive definite, symmetric and strain-driven, is derived. In addition to the degradation parameters, the permanent strain tensor is also contemplated by the model and a modification of the exponential softening modulus is proposed in order to treat the evolution of the two causes of dissipation, damage and irreversible deformations, in a coupled way.

The formulation is integrated with a multidirectional damage procedure, addressed to extend the microcrack closure-reopening (MCR) capabilities of the model to shear cyclic conditions, characterized by orthogonal (or however intersecting) sets of cracks. Maintaining unaltered the dependence of the constitutive law from two scalar indeces, d^+ and d^-, this approach activates or deactivates a tensile (compressive) damage value on the base of the current maximum (minimum) principal strain direction. In correspondence with damage activation (crack opening) or deactivation (crack closure), a smooth transition is introduced, in order to avoid abrupt changes in stiffness and enhance the numerical performance and robustness of the multidirectional procedure. The adequacy of the proposed constitutive model in reproducing experimental results has been proven for both monotonic and cyclic loading conditions. The two examples of application involving cyclic loads, dominated by shear, constitute a validation of the multidirectional

damage approach, showing how the suitable representation of unilateral effects and permanent deformations is essential to model the observed structural response in terms of maximum resistance, evolution of stiffness degradation and dissipation capacity.

Keywords: concrete structures; masonry structures; cracking; damage; damage-induced orthotropy; microcrack closure-reopening effects; cyclic loading; spectral decomposition; energy-equivalence; numerical robustness.

1. Introduction

The engineering modeling of quasi-brittle materials, such as concrete, masonry, rock, ceramics etc., represents a complex issue since several features differentiate their structural response from the one of an isotropic linear elastic material. The pronounced non-symmetrical behavior under tension and compression, with a tensile strength which is very low if compared to the compressive one, is characteristic of quasi-brittle materials. The scarse resistance in tension is responsible for a non-negligible non-linear response even for low stress levels, characterized by microcrack nucleation and growth. Consequently, the cracking phenomenon requires some specific properties to be adequately considered in the constitutive modeling of these materials: besides the softening response in the post-peak regime, these properties are, in accordance with (Caboche, 1992), the damage-induced anisotropy and the microcrack closure-reopening (MCR) effects.

On the one hand, the anisotropy results from the evolution of planar microvoids in the direction perpendicular to the maximum tensile strain, which implies a certain orientation of the stiffness degradation (Krajcinovic, 2003). Such a feature allows one taking into account possible compressive strut action which is unrealistically neglected in isotropic damage models (de Borst, 2002).

On the other hand, microcracks close upon load reversal from tension to compression and a total or partial stiffness recovery has to be simulated in order to realistically capture the hysteretic behavior of the material in cyclic loading conditions (Mazars et al., 1990; Reinhardt and Cornelissen, 1984). This phenomenon is fundamental when the main interest is to perform the analyses of concrete, reinforced concrete or masonry structures under wind and seismic actions (Cervera et al., 1995; Chang and Mander, 1994; Faria et al., 2004; Oliveira, 2003; Xue and Yang, 2014).

In a continuum damage mechanics' framework, a methodology to deal with the asymmetrical performance of quasi-brittle materials under tension and compression

consists in differentiating the response depending on the trace of the strain tensor and in applying different damage variables in tension and compression. Such a procedure is effective in modelling the micro-crack closure reopening effects from pure tension to pure compression but it is not able to simulate any form of damage-induced anisotropy, when scalar damage parameters are adopted (Contraffatto and Cuomo, 2006; Comi and Perego, 2001; He et al., 2015; Toti et al., 2013).

Conversely, as pointed out by Wu and Xu (2013), those formulations based on the spectral decomposition of a specific second order tensor (the stress or the strain one) allows one to reproduce contemporarily unilateral effects and damage-induced anisotropy. This approach, used for the first time in the pioneering work of Ortiz (1985), introduces in the constitutive law two fourth-order projection operators which extract the positive and negative tensor counterparts. A classification of these damage formulations can be performed depending on the nature of the damage variables used in conjunction with the spectral decomposition: one or more scalar damage variables are adopted in (Cervera et al., 1995; Cervera et al., 1996; Faria et al., 1998; Mazars et al., 1990; Wu et al., 2006) whereas models based on second- or fourth-order tensors are presented in (Carol and Willam, 1996; Cicekli et al., 2007; Ju, 1989; Ortiz, 1985; Simo and Ju, 1987; Voyiadjis et al., 2008; Yazdani and Schreyer, 1990).

The continuum damage formulation described in the present work can be included within the first category, since it combines the split of a second-order tensor, specifically the reversible strain one ε_e, with the use of two scalar damage quantities, d^+ and d^-, in order to distinguish tension from compression. Such a choice provides a simplified representation of damage-induced anisotropy and MCR effects, while maintaining adequate predicting capabilities, and makes the model easily implementable in finite element codes and applicable in large-scale simulations at an affordable computational cost, resorting to a strain-driven and explicit formalism.

The main objective of the present paper is to reflect upon some limitations deriving from the adoption of scalar damage variables combined with the spectral decomposition and propose an enhancement of this model. On the one hand, a consistent way to treat damage-induced orthotropy and unilateral effects is presented. On the other hand, the description of permanent deformations is included in the damage model in a coupled dissipative framework. The resulting formulation is validated under monotonic and cyclic loading conditions, highlighting the importance of each model component in the structural response. Under cyclic action, the numerical robustness associated to the modelling of

closure and reopening of cracks is enhanced by the introduction of a smooth transition upon loading reversal.

Regarding the topic of damage-induced anisotropy, a restricted form of orthotropy is described using scalar degradation quantities, since only the projection operators performing the spectral decomposition are responsible for the directionality of the stiffness reduction. As a consequence, the model here described, in analogy with (Cervera et al., 1995; Cervera et al., 1996; Faria et al., 1998; Wu et al., 2006), is characterized by the coincidence between the axes of orthotropy of the damaged materials and the principal directions of the stress tensor during the whole loading history. This "weak degree of anisotropy" is however sufficient to take into account the presence of compressive strut actions (de Borst, 2002).

However, with respect to (Cervera et al., 1995; Cervera et al., 1996; Faria et al., 1998; Wu et al., 2006), a different criterion is exploited in order to relate the constitutive secant stiffness to the damage variables and the projection operators. This criterion is based on the energy-equivalence assumption between nominal and effective configurations (Cordebois et Sidoroff, 1982; Carol et al., 2001) and it is preferred, in thermodynamical terms, to the strain-equivalence hypothesis (Lemaitre and Chaboche, 1978; Simo and Ju, 1987). As observed in (Cervera and Tesei, 2017), it leads to the derivation of an anisotropic secant fourth-order operator that is positive definite and endowed with both major and minor symmetries.

Regarding the description of the unilateral effects, the spectral decomposition approach combined with the adoption of scalar damage variables is effective only in specific cyclic conditions, characterized by alternating tensile and compressive regimes. Hence, if the unilateral behavior is adequately taken into account in a 1D tension compression cyclic history or in bending-dominated cyclic problems (as shown by Faria et al. (2004)), the stiffness recovery in presence of cyclic shear can not be captured. Evidence of this can be provided by considering the problem shown in Fig. 1.a, involving shear cyclic conditions. During the loading stage (Fig.1.b), the internal variable d^+, related to the opening of microcracks perpendicularly to the current maximum tensile direction $\boldsymbol{p}_{max}$, grows up to the value d_I^+. After the loading reversal, at the beginning of the reloading stage (Fig. 1.c), the value d_I^+ is assigned once again to the current $\boldsymbol{p}_{max}$ (which is actually an intact direction) and, consequently, no stiffness recovery is exhibited in the structural response (Fig. 1.d). In other words, due to the scalar nature of the damage variables, the formulation is not able to associate a damage value to a physical direction and this translates in the

incapability of dealing with closure and reopening of orthogonal (or however intersecting) cracks, typical of shear cyclic conditions.

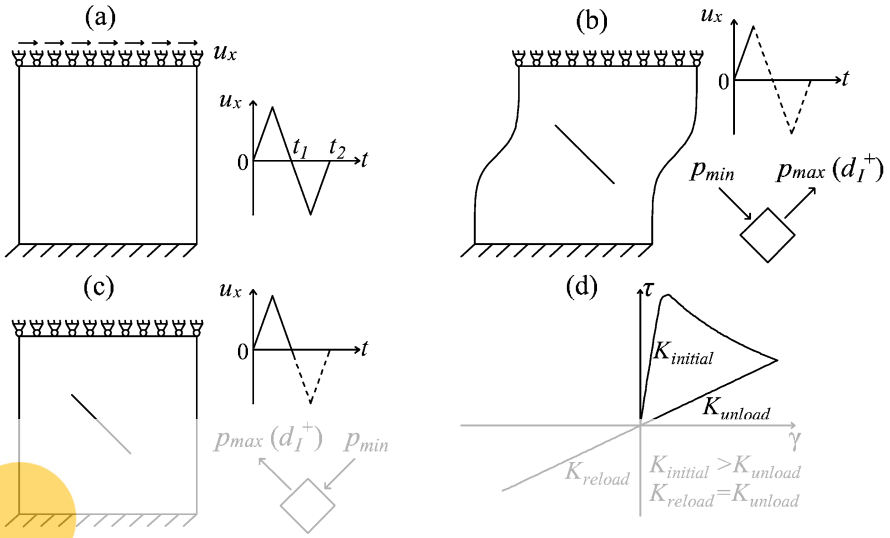

Figure 1 – Limitation of the scalar damage models with spectral decomposition in dealing with cyclic actions.

Such lack of information about damage orientation is comparable to the inability of the rotating crack models (Cope et al., 1980) to take into account the orientation of previous defects, as observed by Bažant (1983). To improve the MCR capabilities of the d^+/d^- damage formulation, the local constitutive behavior of the material needs to incorporate some aspects which are instead proper of fixed crack models (Rots et al., 1985). To this end, a "multidirectional" damage procedure is proposed in the follow up, which preserves memory regarding degradation directionality while maintaining unaltered the dependence of the stress tensor from only the scalars d^+ and d^- (Cervera and Tesei, 2017). In line with this reasoning, it is worth noting that not only the d^+/d^- damage model hereafter presented can take advantage from a multidirectional treatment of damage; potentially, all the orthotropic rotating damage models can be enriched with the multidirectional damage approach.

When treating microcrack closure-reopening effects, a further aspect to be taken into account regards the convergence difficulties arising at structural level. As pointed out in (Jefferson and Mihai, 2015), these numerical difficulties are related to the abrupt changes in the secant stiffness going from an open crack state to a closed one, or vice versa. The multidirectional damage approach is not exempt from these difficulties, since it foresees sudden changes of the active damage values affecting the constitutive law. In order to

increase the numerical robustness of the procedure, a smoothing technique is proposed in the present paper for modelling the activation and deactivation of damage.

Finally, to obtain adequate structural responses in cyclic conditions, another feature to be considered in the modelling of quasi-brittle materials is the development of permanent deformations. In view of this, a simplified as well as effective way to introduce irreversible strains is adopted, in analogy with (Faria et al., 1998). In addition, the two causes of dissipation, permanent deformations and damage, are treated within a unified framework, taking inspiration from (Wu and Cervera, 2016). This translates in the proposal of a modified expression for the softening modulus governing the descending, post-peak, behavior, in presence of permanent strains, which is an adjustment of the linear and exponential softening moduli proposed in (Cervera et al., 1996; Cervera, 2003).

The paper is outlined as follows. In Section 2, the consistent d^+/d^- damage formulation based on the spectral decomposition of the reversible strain tensor ε_e and on the energy-equivalence hypothesis is presented. Specifically, the secant operator ruling the constitutive law, the definition of the irreversible strain rate and of the damage evolution laws are detailed. Appendix A completes this section, showing the passages for the derivation of the modified exponential softening modulus. Section 3 is devoted to the description of the multidirectional damage procedure, to be applied in presence of cyclic loadings, providing some parallels between this new approach and the fixed/rotating smeared crack concepts. The section is enriched with the introduction of a smoothing function, addressed to increase the numerical robustness of the multidirectional procedure in the transition from an open to a close microcrack state (or viceversa). The description of the numerical algorithm adopted for the implementation of the non linear constitutive model is provided in Section 4. Then, the damage formulation, combined with a crack band strategy to prevent mesh dependent results (Bažant and Oh, 1983), is validated in Section 5, considering structural problems involving both monotonic and cyclic loading conditions. Firstly, unreinforced concrete samples are solved under monotonic loadings and the adequacy of the damage formulation based on energy-equivalence in fitting experimental results is shown. Secondly, a masonry wall and a reinforced concrete panel, both subjected to in-plane cyclic shear, are analyzed in order to highlight the enhanced dissipative behavior ensured by the multidirectional damage approach in conjunction with permanent deformations. Some quantitative considerations regarding the numerical robustness of the model are also included. Finally, Section 6 collects the concluding remarks.

2. Mechanical model for quasi-brittle materials

The continuum mechanical model here presented describes the behavior of quasi-brittle materials, including both the stiffness and strength degradation proper of damage and the presence of irreversible deformations. In order to represent these non-linear features, a d^+/d^- damage model based on the irreversible thermo-dynamics with internal variables (Horstemeyer and Bammann, 2010) is proposed, in line with the d^+/d^- formulation developed for concrete by Faria et al. (1998). The internal scalar variables related to damage, d^+ and d^-, together with the spectral decomposition of a second order strain tensor, allow one simulating the asymmetrical behavior typical of quasi-brittle materials under tension and compression, while the tensor internal variable $\boldsymbol{\varepsilon_p}$ represents the permanent strain accumulated during the loading history. The main aspects of the proposed damage formulation are underlined in this section and regard the assumption of energy-equivalence (Section 2.1) between nominal and effective configuration for the derivation of a consistent fourth-order constitutive operator and the use of a coupled dissipative approach to describe the evolution of the internal variables d^+, d^- and $\boldsymbol{\varepsilon_p}$ (Section 2.3 and Appendix A).

2.1 Secant stiffness based on the energy-equivalence assumption

According to the thermodynamics of irreversible processes (Lubliner, 1972), the constitutive law at the base of the present mechanical model is consistently derived starting from a free-energy potential ψ expressed in terms of the independent variable, the nominal strain tensor $\boldsymbol{\varepsilon}$, and the internal variables d^+, d^- and $\boldsymbol{\varepsilon_p}$:

$$\psi\left(\boldsymbol{\varepsilon},\boldsymbol{\varepsilon_p},d^+,d^-\right)=\frac{1}{2}\left(\boldsymbol{\varepsilon}-\boldsymbol{\varepsilon_p}\right):\boldsymbol{D_E}\left(\boldsymbol{\varepsilon}-\boldsymbol{\varepsilon_p},d^+,d^-\right):\left(\boldsymbol{\varepsilon}-\boldsymbol{\varepsilon_p}\right) \tag{1}$$

The dependence of the secant stiffness fourth-order tensor $\boldsymbol{D_E}$ on the damage variables and on the reversible elastic part $\boldsymbol{\varepsilon_e} = \boldsymbol{\varepsilon} - \boldsymbol{\varepsilon_p}$ of the total nominal strain tensor $\boldsymbol{\varepsilon}$ is established by assuming the hypothesis of energy equivalence (Carol et al., 2001; Cordebois and Sidoroff, 1982) between the effective configuration (i.e. the stress $\bar{\boldsymbol{\sigma}}$ and strain $\bar{\boldsymbol{\varepsilon}}$ acting on the undamaged material between microcracks and microvoids, which is considered elastic) and the nominal configuration (i.e. the stress $\boldsymbol{\sigma}$ and reversible strain $\boldsymbol{\varepsilon_e}$ obtained by averaging the corresponding effective quantities on the total surface of the material). Following the procedure described in (Carol et al., 2001), this assumption translates in the following relations:

$$\boldsymbol{\sigma} = \boldsymbol{A}^{*} : \bar{\boldsymbol{\sigma}} \tag{2.a}$$

$$\bar{\boldsymbol{\varepsilon}} = \boldsymbol{A}^{*} : \boldsymbol{\varepsilon}_{\boldsymbol{e}} \tag{2.b}$$

Considering Eq. (2.a), Eq. (2.b) and $\bar{\boldsymbol{\sigma}}$ and $\bar{\boldsymbol{\varepsilon}}$ related by the elastic stiffness operator $\boldsymbol{D_0}$:

$$\bar{\boldsymbol{\sigma}} = \boldsymbol{D_0} : \bar{\boldsymbol{\varepsilon}} \tag{3}$$

the expression for $\boldsymbol{D_E}$ is the following:

$$\boldsymbol{D_E}\left(\boldsymbol{\varepsilon}-\boldsymbol{\varepsilon_p}, d^{+}, d^{-}\right) = \boldsymbol{A}^{*}\left(\boldsymbol{\varepsilon}-\boldsymbol{\varepsilon_p}, d^{+}, d^{-}\right) : \boldsymbol{D_0} : \boldsymbol{A}^{*}\left(\boldsymbol{\varepsilon}-\boldsymbol{\varepsilon_p}, d^{+}, d^{-}\right) \tag{4}$$

The definition for the mapping operator $\boldsymbol{A}^{*}$ is the one proposed in (Cervera and Tesei, 2017):

$$A^{*}\left(\varepsilon_e, d^{+}, d^{-}\right) = \sqrt{1-d^{+}}\,\boldsymbol{Q}(\varepsilon_e) + \sqrt{1-d^{-}}\left[\boldsymbol{I}-\boldsymbol{Q}(\varepsilon_e)\right] \tag{5}$$

From Eq. (5), it is evident that the tensorial nature of the mapping operator $\boldsymbol{A}^{*}$ is provided by the fourth-order projection operators $\boldsymbol{Q}$ and $\boldsymbol{I}-\boldsymbol{Q}$, scaled by the square root of the corresponding integrity quantities. They are responsible for the spectral decomposition of the nominal elastic strain tensor $\boldsymbol{\varepsilon_e}$ into its positive and negative parts, respectively:

$$\boldsymbol{\varepsilon}_{\boldsymbol{e}}^{+} = \sum_{i=1}^{3} \langle \varepsilon_{ei} \rangle \boldsymbol{p}_i \otimes \boldsymbol{p}_i = \boldsymbol{Q} : \boldsymbol{\varepsilon}_{\boldsymbol{e}} \qquad \boldsymbol{\varepsilon}_{\boldsymbol{e}}^{-} = \boldsymbol{\varepsilon}_{\boldsymbol{e}} - \boldsymbol{\varepsilon}_{\boldsymbol{e}}^{+} = (\boldsymbol{I}-\boldsymbol{Q}) : \boldsymbol{\varepsilon}_{\boldsymbol{e}} \tag{6}$$

$$\boldsymbol{Q} = \sum_{i=1}^{3} H(\varepsilon_{ei})\boldsymbol{p}_i \otimes \boldsymbol{p}_i \otimes \boldsymbol{p}_i \otimes \boldsymbol{p}_i + \sum_{\substack{i=1 \\ j>i}}^{3} \left(H(\varepsilon_{ei}) + H(\varepsilon_{ej})\right) \boldsymbol{P}^{ij} \otimes \boldsymbol{P}^{ij} \tag{7}$$

In Eqs. (6) and (7), ε_{ei} and $\boldsymbol{p}_i$ are the principal value and the eigenvector associated to the *i-th* principal direction of $\boldsymbol{\varepsilon_e}$. The Macaulay brackets act on ε_{ei} in such a way that: if ε_{ei} is positive, $< \varepsilon_{ei} > = \varepsilon_{ei}$, else $< \varepsilon_{ei} > = 0$ while $H(\varepsilon_{ei})$ is the Heaviside function, such that, if ε_{ei} is positive, $H(\varepsilon_{ei}) = 1$; else, $H(\varepsilon_{ei}) = 0$. The definition (6) for the projection operator is present in (Carol and Willam, 1996; Wu and Xu, 2013).

The dependence of the mapping operator $\boldsymbol{A}^{*}$(5), i.e. of the secant stiffness matrix $\boldsymbol{D_E}$ (4), on the projection operator $\boldsymbol{Q}$ (7), reflects the fundamental idea of representing the orthotropy induced in the material by the degradation process by means of the spectral decomposition of a second order tensor. Direct consequence of this choice is the coincidence, in a generic case with ε_{ei} of discordant sign, of the axes of orthotropy of the damaged material with the strain $\boldsymbol{\varepsilon_e}$ and the stress $\boldsymbol{\sigma}$ principal directions. Moreover, the energy-equivalence assumption is preferred to the strain-equivalence one (Faria et al., 1998; Simo and Ju, 1987; Wu and Li, 2008) because it guarantees thermodynamic

consistency. In fact, the secant stiffness operator $\boldsymbol{D_E}$ (4) holds both major symmetry and positive definiteness, features which are fundamental for an adequate representation of the damage-induced orthotropy.

2.2 Clausius-Duheim inequality

According to the second law of thermo-dynamics, irreversible processes are characterized by increasing entropy and non-negative dissipated energy. These conditions can be ensured guarantying the satisfaction of the Clausius-Duheim inequality, as stated in (Lubliner, 1972), which is the following:

$$\dot{\gamma} = -\dot{\psi} + \boldsymbol{\sigma} : \dot{\boldsymbol{\varepsilon}} \geq 0 \tag{8}$$

Replacing the total derivative of the energy potential (1) with its partial derivatives with respect to the strain $\boldsymbol{\varepsilon}$ and the internal variables d^+, d^- and $\boldsymbol{\varepsilon_p}$, the inequality (8) becomes:

$$\dot{\gamma} = \left(\boldsymbol{\sigma} - \frac{\partial \psi}{\partial \boldsymbol{\varepsilon}} \right) : \dot{\boldsymbol{\varepsilon}} - \frac{\partial \psi}{\partial d^+} \cdot \dot{d}^+ - \frac{\partial \psi}{\partial d^-} \cdot \dot{d}^- - \frac{\partial \psi}{\partial \boldsymbol{\varepsilon_p}} \cdot \dot{\boldsymbol{\varepsilon}}_p \geq 0 \tag{9}$$

Since $\boldsymbol{\varepsilon}$ is a free variable, in order to have the non-negativeness of the dissipated energy satisfied in the general case, the quantity between round brackets in Eq. (9) has to be null; this results in one of the Coleman's relations (Coleman and Gurtin, 1967) and leads to the establishment of the constitutive law:

$$\boldsymbol{\sigma} = \frac{\partial \psi}{\partial \boldsymbol{\varepsilon}} = \boldsymbol{D_E} : \boldsymbol{\varepsilon_e} \tag{10}$$

Hence, the Clausius-Duheim inequality reduces to:

$$\dot{\gamma} = -\frac{\partial \psi}{\partial d^+} \cdot \dot{d}^+ - \frac{\partial \psi}{\partial d^-} \cdot \dot{d}^- - \frac{\partial \psi}{\partial \boldsymbol{\varepsilon_p}} : \dot{\boldsymbol{\varepsilon}}_{\boldsymbol{p}} \geq 0 \tag{11}$$

From Eq. (11), it is evident that the dissipative behaviour of the material is due to both damage evolution and generation of permanent strains. On the one hand, the derivatives of the free energy potential with respect to d^+ and d^-, with sign reversed, represent the strain-energy release rates associated to a unit growth of the corresponding damage variables. The full expressions for these quantities, as well as the discussion on the non-negativeness of the energy dissipated due to damage evolution, are provided in (Cervera and Tesei, 2017). On the other hand, the derivative of the free energy with respect to $\boldsymbol{\varepsilon_p}$,

with sign reversed, coincides with the nominal stress $\boldsymbol{\sigma}$ and plays the role of a thermodynamic force associated to the permanent strain; the non-negativeness of the energy dissipated by this quantity is proven in Section 2.3.1, where the definition of the permanent strain rate $\dot{\varepsilon}_p$ is provided. The positiveness of all the terms present in Eq. (11) will allow concluding on the consistency of the proposed damage model for what regards the second principle of thermo-dynamics. Moreover, the satisfaction of the first principle of thermodynamics is stated in (Cervera and Tesei, 2017).

2.3 Internal variables

2.3.1 Permanent strains

The modeling of permanent strains is relevant in the prediction of the structural behavior of concrete and quasi-brittle materials in general, since during a loading history irreversible strains accumulate, affecting in a non-negligible way both strength and stiffness. A simplified way of taking into account permanent strains, which is a modification of the one adopted in (Faria et al., 1998), is here proposed, without the necessity of introducing concepts as the plasticity surface or the flow rule:

$$\dot{\boldsymbol{\varepsilon}}_p = \left[b^+ \cdot H\left(\dot{d}^+\right) + b^- \cdot H\left(\dot{d}^-\right) \right] \frac{\langle \boldsymbol{\sigma}_e : \dot{\boldsymbol{\varepsilon}} \rangle}{\boldsymbol{\sigma}_e : \boldsymbol{\varepsilon}_e} \cdot \boldsymbol{\varepsilon}_e \tag{12}$$

In Eq. (12), b^+ and b^- are two positive material parameters defining the entity of the permanent strains under tensile and compressive regimes, ranging from 0 (only damage) to 1; regarding the tensor quantities, $\dot{\boldsymbol{\varepsilon}}$ is the total strain rate, $\boldsymbol{\varepsilon}_e$ is the reversible strain and $\boldsymbol{\sigma}_e$ is the elastic stress tensor, whose expression is:

$$\boldsymbol{\sigma}_e = \boldsymbol{D}_0 : \boldsymbol{\varepsilon}_e \tag{13}$$

The ratio between the elastic power $\boldsymbol{\sigma}_e : \dot{\boldsymbol{\varepsilon}}$ and the double of the elastic strain energy $\boldsymbol{\sigma}_e : \boldsymbol{\varepsilon}_e$ contributes to define the intensity of the plastic strains. The simplifications with respect to a plastic theory are recognizable in Eq. (12): instead of the adoption of a flow rule, the irreversible strain evolves in the direction of the elastic strain tensor $\boldsymbol{\varepsilon}_e$ and of the elastic stress tensor $\boldsymbol{\sigma}_e$. This is coherent with the definition of the evolution of damage in terms of the elastic stress values, as discussed in Section 2.3.2.

In addition, the same conditions holding for damage progression are taken into account for the permanent strain evolution and this relation is established by means of the Heaviside functions $H\left(\dot{d}^+\right)$ and $H\left(\dot{d}^-\right)$. With respect to the proposal made in (Faria et

al., 1998), the development of irreversible deformations is not only associated to compressive regimes but the possibility of permanent strain evolution under tensile regimes is also considered. This choice is addressed to catch more realistic results both in pure tension and in case of coexistence of compressive and tensile regimes, i.e. in shear conditions.

Moreover, referring to the definition here provided for $\dot{\boldsymbol{\varepsilon}}_{\boldsymbol{p}}$ (12), the quantity $-\frac{\partial \psi}{\partial \boldsymbol{\varepsilon}_{\boldsymbol{p}}} : \dot{\boldsymbol{\varepsilon}}_{\boldsymbol{p}}$, appearing in Eq. (11) can be expressed in the following way

$$\begin{aligned} -\frac{\partial \psi}{\partial \boldsymbol{\varepsilon}_{\boldsymbol{p}}} : \dot{\boldsymbol{\varepsilon}}_{\boldsymbol{p}} = \boldsymbol{\sigma} : \dot{\boldsymbol{\varepsilon}}_{\boldsymbol{p}} = \boldsymbol{D}_{\boldsymbol{E}} : \boldsymbol{\varepsilon}_{\boldsymbol{e}} : \left[b^{+} \cdot H\left(\dot{d}^{+}\right) + b^{-} \cdot H\left(\dot{d}^{-}\right) \right] \frac{\left\langle \boldsymbol{\sigma}_{\boldsymbol{e}} : \dot{\boldsymbol{\varepsilon}} \right\rangle}{\boldsymbol{\sigma}_{\boldsymbol{e}} : \boldsymbol{\varepsilon}_{\boldsymbol{e}}} \cdot \boldsymbol{\varepsilon}_{\boldsymbol{e}} \\ = a \cdot \boldsymbol{D}_{\boldsymbol{E}} : \boldsymbol{\varepsilon}_{\boldsymbol{e}} : \boldsymbol{\varepsilon}_{\boldsymbol{e}} = 2 \cdot a \cdot \psi \end{aligned} \tag{14}$$

where the scalar a is:

$$a = \left[b^{+} \cdot H\left(\dot{d}^{+}\right) + b^{-} \cdot H\left(\dot{d}^{-}\right) \right] \frac{\left\langle \boldsymbol{\sigma}_{\boldsymbol{e}} : \dot{\boldsymbol{\varepsilon}} \right\rangle}{\boldsymbol{\sigma}_{\boldsymbol{e}} : \boldsymbol{\varepsilon}_{\boldsymbol{e}}} \tag{15}$$

Since a (15) is non-negative and the free energy potential (1) is a quadratic form ruled by the positive definite secant stiffness $\boldsymbol{D}_{\boldsymbol{E}}$, the quantity contained in (14), i.e. the energy dissipated due to irreversible deformations, is non-negative and this assures the satisfaction of the Clausius-Duheim inequality (11) discussed in Section 2.2.

2.3.2 Damage variables

The definition and progression of the tensile and compressive damage variables is treated separately, by means of independent equivalent stress quantities $\tau \pm$, independent damage thresholds $r \pm$ and independent damage evolution laws.

In analogy with (Petracca et al., 2017; Saloustros et al., 2017), the failure criterion considered as reference for the definition of the damage surface is the one proposed in (Lubliner et al., 1989) for concrete. The definitions for the equivalent stress quantities, monitoring the strain-stress state under tension and under compression, are the following:

$$\tau^{+} = H\left(\sigma_{emax}\right) \frac{1}{1-\alpha} \frac{f_e^{+}}{f_e^{-}} \left(\sqrt{3J_2} + \alpha I_1 + \beta \left\langle \sigma_{emax} \right\rangle \right) \tag{16.a}$$

$$\tau^{-} = H\left(-\sigma_{emin}\right) \frac{1}{1-\alpha} \left(\sqrt{3J_2} + \alpha I_1 + \beta \left\langle \sigma_{emax} \right\rangle \right) \tag{16.b}$$

where the material strength parameters α and β, defined accordingly to (Lubliner et al., 1989), are:

$$\alpha = \frac{(f_b^- / f^-) - 1}{2(f_b^- / f^-) - 1} \qquad \beta = (1-\alpha)\frac{f_e^-}{f_e^+} - (1+\alpha) \tag{17}$$

In expressions (16), I_1, J_2, σ_{emax} and σ_{emin} are the first invariant, the deviatoric second invariant, the maximum and minimum principal values referred to the elastic stress tensor $\boldsymbol{\sigma_e}$ defined in Eq. (13). The choice of adopting the elastic stress tensor (13), instead of the effective one (3), in Eqs. (12), (16.a), (16.b) allows to avoid the recourse to an iterative procedure in the evaluation of the internal variables. In fact, the computation of $\boldsymbol{\sigma_e}$ is straightforward and follows directly from the computation of the nominal elastic strain tensor $\boldsymbol{\varepsilon_e}$. The other parameters appearing in Eqs. (16) and (17) are the uniaxial tensile and compressive peak strengths of the material f^+ and f^-, the biaxial compressive strength f_b^- and the values f_e^+ and f_e^-, which define the onset of damage in uniaxial tension and compression respectively, by means of the proportional parameters γ_e^+ and γ_e^- ($0 < \gamma_e^{\pm} \leq 1$):

$$f_e^{\pm} = \gamma_e^{\pm} f^{\pm} \tag{18}$$

In order to distinguish among loading, unloading or reloading, the Kuhn-Tucker relations and the persistency conditions are considered:

$$\dot{r}^{\pm} \geq 0 \qquad g^{\pm} = \tau^{\pm} - r^{\pm} \leq 0 \qquad \dot{r}^{\pm} \cdot g^{\pm} = 0 \tag{19.a}$$

$$\dot{r}^{\pm} \cdot \dot{g}^{\pm} = 0 \tag{19.b}$$

$g^{\pm} = 0$ is the damage limit surface, increasing in size in case of loading ($g^{\pm} = 0$, $\dot{r}^{\pm} > 0$) and remaining unchanged during the unloading or in the undamaged situation ($g^{\pm} < 0$, $\dot{r}^{\pm} = 0$). The definition for the non-decreasing functions $r^{\pm}$, representing the damage thresholds, can be inferred by imposing $\dot{g}^{\pm} = 0$, necessary condition for satisfying Eq. (19.b) in the loading case:

$$r^{\pm} = \max\left(r_0^{\pm}; \max_{[0,t]}\left(\tau^{\pm}\right) \right) \tag{20}$$

where:

$$r_0^{\pm} = f_e^{\pm} \tag{21}$$

and $\max(\tau^{\pm})$ represents the maximum value until the current instant t.

As visible from Eqs. (19), the shape of the damage limit surface $g^{\pm} = 0$ depends on the specific choice done for the equivalent quantities $\tau^{\pm}$. By referring to Eqs. (16.a) and (16.b), the initial damage surface shown in Fig. 2 for the plane stress case is obtained.

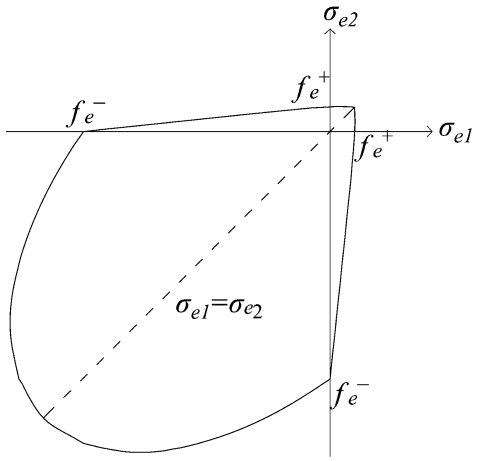

Figure 2 – Initial damage surface in plane stress conditions, for $\alpha = 0.121$, $\beta = 7.667$.

In pure tension (1st quadrant) and pure compression (3rd quadrant), the surface is affected only by τ^+ and τ^- respectively, meaning that only d^+ can be activated in the 1st quadrant and only d^- in the 3rd quadrant. Differently, when principal stress values with opposite signs are present (2nd and 4th quadrants), the same damage surfaces are identified by τ^+ and τ^- and the activation of tensile and compressive damage is simultaneous.

For what regards the evolution laws of the internal variables d^+ and d^-, they are defined as non-decreasing functions of the thresholds quantities r^+ and r^-, taking inspiration from the trends proposed in (Cervera, 2003), which simulate both a parabolic hardening stage and an exponential softening one:

$$d^{\pm}\left(r^{\pm}\right) = A_d^{\pm}\frac{f^{\pm}}{r^{\pm}}\left(\frac{r^{\pm}-r_0^{\pm}}{f_p^{\pm}-r_0^{\pm}}\right)^2 \qquad r_0^{\pm} \le r^{\pm} \le f_p^{\pm} \tag{22.a}$$

$$d^{\pm}\left(r^{\pm}\right) = 1-\frac{f^{\pm}}{r^{\pm}}\cdot\exp\left(2H_d^{\pm}\cdot\left(\frac{f_p^{\pm}-r^{\pm}}{f^{\pm}}\right)\right) \qquad r^{\pm} > f_p^{\pm} \tag{22.b}$$

The introduction of two further variables f_p^+ and f_p^-, representing the equivalent quantities for which the maximum peak strength is attained, is necessary ($\gamma_p^{\pm} \ge 1$):

$$f_p^{\pm} = \gamma_p^{\pm} f^{\pm} \tag{23}$$

Moreover, the definitions for the parameter A_d and the exponential softening modulus H_d are the following:

$$A_d^{\pm} = \frac{f_p^{\pm} - f^{\pm}}{f^{\pm}} \tag{24}$$

$$\frac{1}{2H_d^{\pm}} = \left(1 - b^{\pm}\right)\left(\frac{EG_f^{\pm}}{\left(f^{\pm}\right)^2} \frac{1}{l_{dis}} - \frac{1}{2}\frac{f_p^{\pm}}{f^{\pm}} - \bar{A}_d^{\pm} - \frac{b^{\pm}}{1-b^{\pm}} \tilde{A}_d^{\pm} \right) \tag{25}$$

In the definition (25) of the softening modulus $2H_{\mathrm{d}}{}^{\pm}$ governing the descending exponential behavior, the presence of the fracture energies $G_f{}^{\pm}$ and of the length l_{dis}, representing the crack width and related to the discretization (see (Oliver, 1989)), assures mesh-size objective results, in accordance with the crack band theory presented in (Bažant and Oh, 1983).

The realistic assumptions done for the values of $\gamma_e{}^{\pm}$ (Eq. (18)) and $\gamma_p{}^{\pm}$ (Eq. (23)) in case of quasi brittle materials are the following: in tension, $\gamma_{e^+} = 1 = \gamma_{p^+}$; in compression, the parabolic hardening before the attainment of f^- is taken into account, meaning that $\gamma_{e^-} < 1 < \gamma_{p^-}$.

Other parameters affecting the damage evolution, visible in (25), are $b^{\pm}$, i.e. the material parameters introduced in the evaluation of the permanent strain rate $\dot{\boldsymbol{\varepsilon}}_{\boldsymbol{p}}$ (12) and defining the intensity of the irreversible deformations. This choice is addressed to consider the two causes of dissipation identified in the Clausius-Duheim inequality (11), which are the progression of damage and the development of permanent strains, within a unified approach. Eq. (25) represents a modification with respect to the exponential softening modulus provided in (Cervera et al., 1996; Cervera, 2003), whose expression is:

$$\frac{1}{2H_d^{\pm}} = \left(\frac{EG_f^{\pm}}{\left(f^{\pm}\right)^2} \frac{1}{l_{dis}} - \frac{1}{2}\frac{f_p^{\pm}}{f^{\pm}} - \bar{A}_d^{\pm} \right) \tag{26}$$

The details regarding the derivation of the new version of the exponential softening modulus (25) and the full expressions of all the terms appearing in Eq. (25) are provided in Appendix A, together with further observations on the topic.

The uniaxial σ-ε curves for a loading-unloading history in pure tension and pure compression are displayed in Fig. 3.a and Fig. 3.b, respectively. In each graph, the responses obtained with both the softening modulus (25) and (26) are collected, in order to have further insight on the influence that the parameters $b^{\pm}$ have on the non-linear behavior. The objective of the correction here provided to the softening modulus (Eq. (25)) is evident and consists in avoiding over dissipation of energy: for a given amount

of irreversible deformations, i.e. for a given $b^{\pm}$, the adoption of Eq. (25) with respect to Eq. (26) causes a steepest softening response. As observed in Appendix A, this allows maintaining the same dissipated energy with or without irreversible deformations, compensating the additional dissipative contribution due to permanent strains with a reduced contribution related to damage.

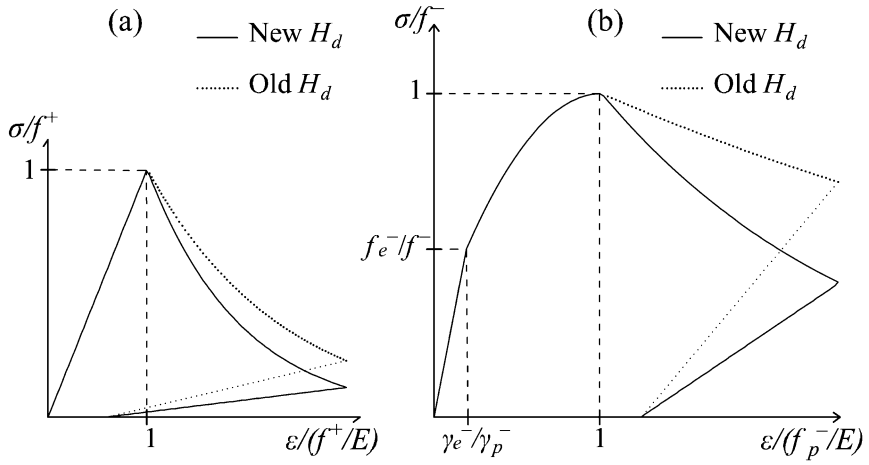

Figure 3 – 1D loading – unloading behavior of the material **(a)** in tension and **(b)** in compression, showing the difference between the new version of the softening modulus (25) and the old one (26).

3. Multidirectional d^+/d^- damage procedure for cyclic loadings: formulation and numerical aspects

In order to overcome the limitation of scalar damage formulations to simulate MCR effects in shear cyclic conditions (Fig. 1), the constitutive model presented in Section 2 is enriched with a "multidirectional d^+/d^- damage procedure", able to ensure the preservation of memory regarding microcracks orientation, without the necessity of resorting to a tensor definition for damage.

In this section, the fundamental aspects of this new approach, formulated in (Cervera and Tesei, 2017), are summarized, making reference, for the sake of clarity and without loss of generality, to plane problems. Moreover, the synergy between the multidirectional damage approach and the definition provided in Eq. (12) for the permanent strain tensor is underlined, showing how their combined adoption affects favorably the structural dissipative behavior under cyclic shear conditions. Then, an interesting interpretation of the multidirectional damage approach is provided by establishing some parallels with the concepts of fixed, multi-directional fixed and rotating crack models (Rots and Blaauwendraad, 1989). To complete the section, a numerical regularization technique of the multidirectional procedure is proposed, addressed to improve the convergence in correspondence of closure and reopening of cracks.

3.1 Formulation of the multidirectional damage model

At the base of the "multidirectional d^+/d^- damage model", there is the idea of considering two independent damage evolution processes for tension and two independent damage evolution processes for compression, differing for the direction in which they act. This translates in the necessity of monitoring separately two damage values in tension and two damage values in compression and this is performed by means of a plane partition into two regions for d^+ and two regions for d^-. Each region is endowed with its own (tensile or compressive) degradation parameter d and damage threshold r. The assignment of a tensile (compressive) damage value to a certain region occurs on the base of the maximum (minimum) principal strain direction which has caused it; specifically, the reference tensor quantity is the elastic strain $\boldsymbol{\varepsilon_e}$, in order not to alter the strain-driven formalism followed in the evaluation of the secant matrix and of the internal variables (Section 2.1 and Section 2.3, respectively).

The active value of d^+ (d^-), i.e. the one affecting the constitutive law (10), is computed starting from the internal variables d^+ and r^+ (d^- and r^-), associated to the damage region in which the current maximum (minimum) principal strain direction falls. In order not to compromise the irreversibility of the damage process, the updating of the active damage values is performed taking into account, within each region, the Kuhn-Tucker and persistency conditions (19) and the monotonically increasing evolution laws (22). The inactive damage values are however kept in memory with the possibility of being re-activated in correspondence of a principal directions' rotation.

In analogy with (Cervera and Tesei, 2017), the distinction between two families of cyclic loading conditions is herein considered:

i. Cyclic loadings characterized by a fixed principal reference system and by changes of the principal configuration only in presence of load reversal; this is the case in a 1D cyclic history or in pure shear cyclic conditions, when the rotation of the principal directions is represented by a swapping between minimum and maximum principal directions.
ii. Cyclic loadings with continuous rotation of maximum and minimum principal directions; this is the case of cyclic histories preceded by non negligible not-cyclic loadings.

It is important to underline that the multidirectional concepts above described, based on the monitoring of damage depending on its orientation, hold for both the types of loading. As discussed in the follow-up, the differences mainly lie in the way according to which

the damage regions are identified during the loading history, and consequently, in the stiffness recovery capabilities which could be modeled.

3.1.1 Load Type (i)

Regarding load Type (i), since, except changes in correspondence of load reversal, the principal directions are fixed during the loading history, also the damage regions in tension and compression in which the space is divided are considered fixed: their bisectors are assumed coincident with the principal reference system ($\boldsymbol{p}_{max\_d}$, $\boldsymbol{p}_{min\_d}$) in correspondence of which damage occurs for the first time and their amplitude is equal to $\pi/2$:

$$\begin{aligned} \boldsymbol{bisector}_1^+ &= \boldsymbol{p}_{max\_d} \quad \boldsymbol{bisector}_2^+ = \boldsymbol{p}_{min\_d} \quad amplitude_{1,2}^+ = \pi/2 \\ \boldsymbol{bisector}_1^- &= \boldsymbol{p}_{min\_d} \quad \boldsymbol{bisector}_2^- = \boldsymbol{p}_{max\_d} \quad amplitude_{1,2}^- = \pi/2 \end{aligned} \tag{27}$$

The orthogonality between the bisectors of the tensile (compressive) damage regions, visible in Eq. (27), allows assuming that the full fracture energy G_f^+ (G_f^-) is consumed in each tensile (compressive) region, independently from one other. When a change of the principal configuration occurs for the first time after the plane partition, i.e. after appearance of damage, two situations are contemplated: if the rotation is significant, for instance equal to $\pi/2$ in case of swapping between maximum and minimum principal directions, a complete regain of the initial stiffness is assured; if the rotation is not relevant, and lower than $\pi/4$, there is no switching from a region to the other one, and no unilateral effects are visible in the structural response.

The problems which can be treated according to this procedure are mainly represented by structural elements in which permanent loads are negligible with respect to variable loads with cyclic nature, as wind and seismic actions.

To clarify the bases of the multidirectional approach in case of load Type (i), the problem of pure shear cyclic loading is considered at a local level (see Fig. 4.a). It can be classified as load Type (i) since, as visible from Fig. 4.b, the angle between the maximum principal elastic strain direction θ and the horizontal axis is fixed during the loading history, except at loading reversal (instant t_1), when a swapping between the maximum and minimum principal directions occurs. The response obtained with the adoption of the multidirectional damage model is shown in Fig. 4.c: differently from the curve in Fig. 1.d, here a complete stiffness recovery is clearly visible after loading reversal. Such a result is achieved by partitioning the plane, according to Eq. (27), in the way illustrated in

Fig. 4.d and Fig. 4.e, which represent the tensile and compressive damage regions, respectively. Before loading reversal, the active damage values are the ones related to tensile and compressive damage regions 1 (as indicated in Fig. 4.d and Fig. 4.e), while, after the rotation of the principal directions, they become the ones associated to regions 2.

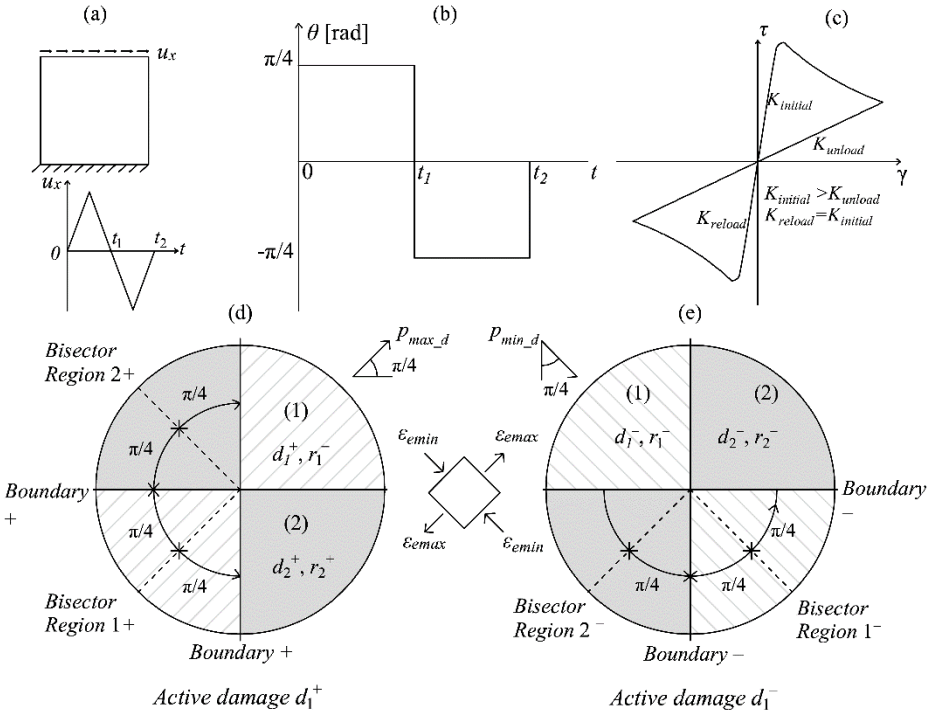

Figure 4 – Load Type (i) problem depicted in **(a)**: **(b)** typical rotation of the principal maximum direction during the loading history; **(c)** local response under shear cyclic action; identification of the **(d)** tensile and **(e)** compressive damage regions·

3.1.2 Load Type (ii)

Regarding load Type (ii), the continuous rotation of the principal directions and the oscillation around the initial configuration requires the adoption of a criterion for defining the activation of a multidirectional damage approach and the consideration of evolving, non-fixed, damage regions. To do this, the introduction of two sets of variables is performed, monitoring the deviation of the principal reference system with respect to the initial conditions; the definition of the first set of variables, the equivalent deviation quantities $\tau^{\pm}{}_{\theta}$, is the following:

$$\tau_{\theta}^{\pm} = \cos\left(\theta_{\tau}^{\pm}\right) \tag{28}$$

where $\theta^{+}{}_{\tau}$ ($\theta^{-}{}_{\tau}$) represents the absolute value of the angle between the current maximum (minimum) principal strain direction and the initial maximum (minimum) principal strain direction, ranging from 0 to π/2.

The second set of variables is constituted by the threshold deviation quantities $r^{\pm}_{\theta}$, which can be computed according to the expression:

$$r_{\theta}^{\pm} = \cos\left(\theta_r^{\pm}\right) = \min\left(\cos\left(\theta_{min}\right); \min_{[0,t]}\left(\tau_{\theta}^{\pm}\right)\right) \tag{29}$$

From Eq. (29), it results that θ^{+}_{r} (θ^{-}_{r}) represents the maximum value assumed by the equivalent angle θ^{+}_{τ} (θ^{-}_{τ}) until the current time t, provided that it is higher than the minimum threshold deviation θ_{min} This parameter assumes the important role of the minimum deviation angle for which an independent treatment of the damage variable is valid. The analogy between the definition of the damage threshold $r^{\pm}$ (20) and the deviation threshold $r^{\pm}_{\theta}$ (29) is evident: as r^{+} (r^{-}) rules the evolution of the damage variable d^{+} (d^{-}), as r^{+}_{θ} (r^{-}_{θ}) governs the evolution of the damage regions, in terms of their bisector and their amplitude. Specifically:

$$\begin{aligned} &\boldsymbol{bisector}^{\pm}_{1,2} = \pm\theta_r^{\pm} \quad amplitude^{+}_{1,2} = 2\cdot\theta_r^{\pm} \quad if\ \theta_r^{\pm} \le \pi/4 \\ &\boldsymbol{bisector}^{\pm}_{1,2} = \pi/4 \quad amplitude^{+}_{1,2} = \pi/2 \quad if\ \theta_r^{\pm} > \pi/4 \end{aligned} \tag{30}$$

where $\boldsymbol{bisector}^{+}_{1,2}$ ($\boldsymbol{bisector}^{-}_{1,2}$) refer to the directions evaluated starting from the initial maximum $\boldsymbol{p}_{max\_0}$ (minimum $\boldsymbol{p}_{min\_0}$) principal strain direction. As visible in Eq. (30), the amplitude of each region increases with the evolution of the region's bisector: this translates in the fact that two directions initially belonging to the same damage region continue to be affected by the same degradation parameter during the whole loading history. Moreover, due to the orthogonality between maximum and minimum principal directions, $\tau^{+}_{\theta} = \tau^{-}_{\theta}$ and $r^{+}_{\theta} = r^{-}_{\theta}$; hence, the activation of the multidirectional procedure and the updating of the damage regions in tension and in compression, whose conditions are expressed in Eqs. (31), occur simultaneously. For this reason, hereafter, the superindex $\pm$ is neglected.

$$\dot{r}_{\theta} \le 0 \qquad g_{\theta} = \tau_{\theta} - r_{\theta} \ge 0 \qquad \dot{r}_{\theta} \cdot g_{\theta} = 0 \qquad \dot{r}_{\theta} \cdot \dot{g}_{\theta} = 0 \tag{31}$$

Once again, a similarity between the conditions (31) and (19) ruling the updating of the damage variables is present. According to Eqs. (31), four different situations can be distinguished:

- $g_{\theta} > 0$, $\dot{r}_{\theta} = 0$ and $r_{\theta} = \cos(\theta_{min})$: the multidirectional procedure is not active since the equivalent deviation angle θ_{τ} (28) has never overcome the minimum deviation θ_{min} .

The value of d^+(d^-) is the same in both the tensile (compressive) damage regions, identified according to Eq. (30);

- $g_\theta = 0$, $\dot{r}_\theta < 0$ and $\theta_r < \pi/4$ (loading conditions): the multidirectional procedure is active and the bisectors of the damage regions rotate, accompanied by an increase of the regions' amplitude, according to Eq. (30);
- $g_\theta = 0$, $\dot{r}_\theta < 0$ and $\theta_r \geq \pi/4$ (loading conditions): the multidirectional procedure is active but the damage regions do not evolve, according to Eq. (30), to avoid overlapping;
- $g_\theta > 0$, $\dot{r}_\theta = 0$ and $r_\theta < \cos(\theta_{min})$ (unloading conditions): the multidirectional procedure is active and the damage regions coincide with the ones assumed at the last loading step.

From the above considerations, the introduction of a minimum threshold deviation θ_{min} allows to simulate three different situations in presence of load Type (ii): if the cyclic conditions do not generate significant deviations from the initial principal configuration, the multidirectional damage approach is not activated and no unilateral effects are taken into account; if the multidirectional procedure is activated and some damage is already present, the model holds partial stiffness recovery capabilities; finally, if the multidirectional procedure is activated without any damage already present, total stiffness recovery is assured.

Conversely to load Type (i), this procedure allows to model situations in which permanent loads are non-negligible with respect to variable cyclic loads.

For the sake of clarity, a problem identifiable as load Type (ii) is solved with the multidirectional approach. Specifically, the case of a panel subjected first to a vertical pre-contraction and then to a cyclic horizontal displacement on the top side is taken into account (Fig. 5.a). The continuous rotation of the maximum principal elastic strain direction with respect to the initial configuration ($\boldsymbol{p}_{max\_0}$), coincident with the x-axis, is shown in Fig. 5.b in terms of the deviation θ. Except for the positive and negative sign, this curve represents the trend of the equivalent quantity θ_τ (see Eq. (28)), which coincides with the absolute value of the actual deviation angle θ. Since θ overcomes the minimum threshold θ_{min}, the resulting τ - γ curve, Fig. 5.c, shows shear stiffness recovery after loading reversal (instant t_1). Due to the evolving nature of the damage regions, foreseen by the multidirectional procedure in case of rotating principal directions (Fig. 5.b), the plane partition changes during the loading history. In particular, the one depicted in Fig. 5.d and Fig. 5.e refers to the specific loading time t_{max1}, i.e. the instant associated

with the maximum rotation $\theta_{max} < \pi/4$. Since this case corresponds to a loading condition ($g_\theta = 0$, $\dot{r}_\theta < 0$ and $\theta_r < \pi/4$), in accordance with Eq. (30), ***bisector***$^{+}{}_{1}$ coincides with the principal direction $\boldsymbol{p}_{max}$ associated to ε_{max} while ***bisector***$^{-}{}_{1}$ coincides with $\boldsymbol{p}_{min}$ associated to ε_{min}. Similarly to the case of load Type (i), the description of the MCR effects is ensured by the transition from a damage region to the other one, occurring in correspondence of load sign reversal.

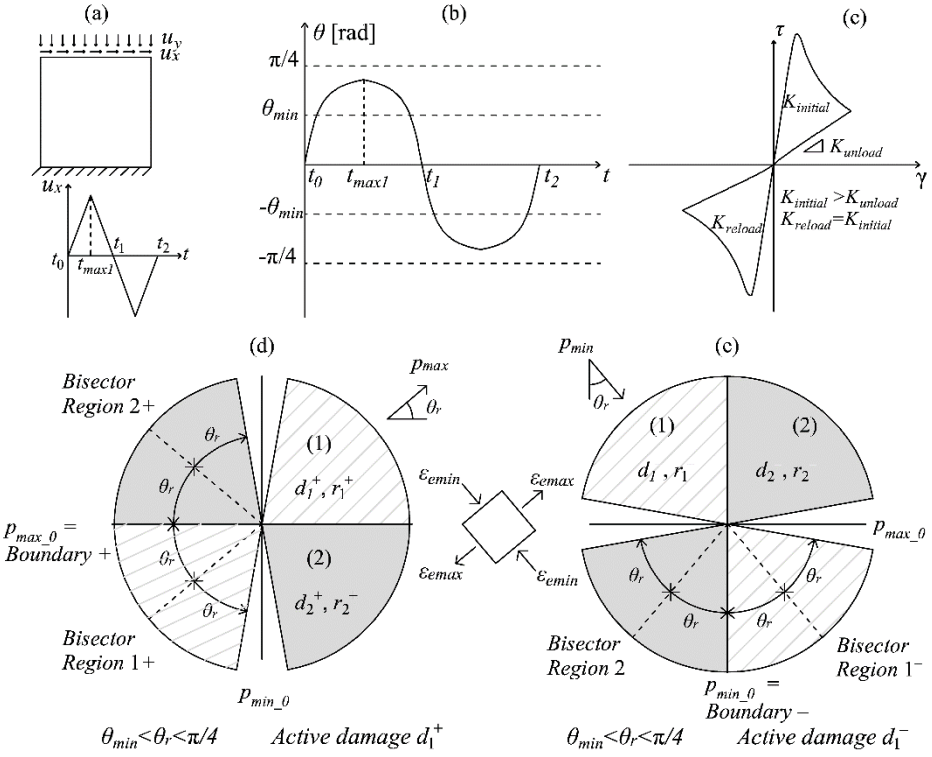

Figure 5 –Load Type (ii) problem depicted in **(a)**: **(b)** typical continuous rotation of the maximum principal direction during the loading history; **(c)** local response under cyclic shear action with pre-contraction; identification of the **(d)** tensile and **(e)** compressive damage regions in loading conditions.

3.2 Enhanced dissipative behavior under cyclic conditions

The versatility of the multidirectional damage approach in modelling a partial or complete stiffness regain in shear cyclic conditions has been extensively discussed in (Cervera and Tesei, 2017). A further positive aspect deriving from the adoption of the multidirectional procedure is here highlighted by solving at a finite element level the problem of a panel subjected to in-plane cyclic shear, classified as load Type (i) (see Fig. 1 and Fig. 4). The analyzed loading history is composed of five complete cycles of loading and reloading, with increasing amplitude, and the structural responses obtained with the multidirectional procedure (Fig. 6a) and without the multidirectional procedure (Fig. 6b) are compared.

Besides the unilateral capabilities appreciable in Fig. 6.a, particularly evident in the elastic stiffness recovery at the beginning of the first reloading stage, another effect strictly related to the adoption of the multidirectional procedure is the more adequate representation of the evolution of permanent deformations under cyclic shear. Here, the possibility of differentiating the damage processes depending on the orientation of the principal strain directions reflects in taking into account, realistically, the energy dissipated in the formation of both the orthogonal cracks. This translates in considering the active damage values increasing even after loading reversal and has, as consequence, the accumulation both in loading and reloading of the permanent strains (12), defined on the base of $\dot{d}^+$ and $\dot{d}^-$ (see Fig. 6.a). Contrarily, in a pure scalar damage formulation, the lack of unilateral effects in shear conditions implies, due to Eq. (12), an underestimation of the irreversible deformations in the reloading stages (see Fig. 6.b).

These enhanced dissipative capabilities under cyclic conditions ensured by the proposed multidirectional damage model are further underlined in the section devoted to structural applications, where the comparison with experimental data is provided.

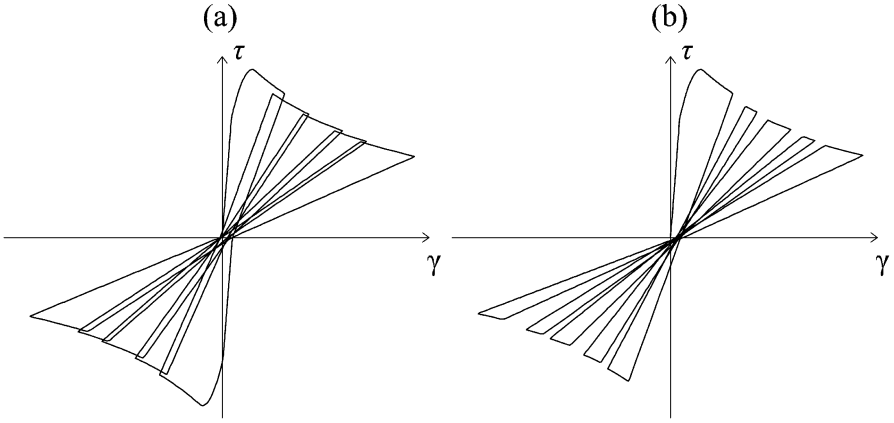

Figure 6 – Cyclic response for the pure shear problem depicted in Fig. (1.a) (a) with the multidirectional procedure and (b) without the adoption of the multidirectional procedure.

3.3 Parallels among the multidirectional damage model and fixed/rotating smeared crack concepts

The consistent damage model proposed in section 2 fits within the framework of the rotating smeared crack concept, introduced for the first time in (Cope et. al, 1980). In fact, as outlined in Section 2.1, the alignment between the axes of orthotropy of the damaged material and the principal strain directions is a feature of the proposed orthotropic damage model. Moreover, the limitations observed in the modelling of MCR effects in presence of shear cyclic loading (Fig. 1) are comparable to the inability of the rotating crack models to take into account the orientation of previous defects. As stated in the Introduction, the

inclusion of the procedure described in Section 3.1 consists in enriching the damage formulation with some properties proper of the fixed crack models (Rots et al., 1985), specifically the preservation of memory regarding damage orientation. Rather than to a pure fixed crack model, the present proposal can be assimilated to a multidirectional fixed crack model (de Borst and Nauta, 1985; Riggs and Powell, 1986; Rots and Blaauwendraad, 1989).

First of all, a similar use of a threshold angle is present in the multidirectional damage model and in the multidirectional fixed crack model. As in the former, the transition between two different damage values is performed only when a rotation of the principal directions greater than a certain angle occurs, in the latter, a new crack is initiated only when the inclination of the principal directions with respect to existing cracks overcomes a certain threshold. Moreover, some specific hypotheses discussed in (Rots and Blaauwendraad, 1989) for the implementation of a multidirectional model are in good agreement with the choices here done in the modelling of the multidirectional damage. In fact, the assumption to consider the value of the damage variables evolving in a region independently of what happens in the other region is analogous to consider the behaviour of each multidirectional crack as the one of a single crack. In view of this, adequate values for θ_{min}, the minimum threshold deviation appearing in Eq. (29), can be chosen in accordance with (Rots and Blaauwendraad, 1989) and range between $\pi/12$ and $\pi/6$.

In addition, the choice of considering only one active value of damage in tension and one in compression is in line with the hypothesis done in multidirectional models of adopting the most recent initiated defect as the only currently-active crack. This is supported by experimental evidence: only the most recently initiated crack is active in a system of non-orthogonal defects (Vecchio and Collins, 1986). A difference between the multidirectional fixed crack concept and the multidirectional damage model lies in the fact that the former deals with a collection of several fixed defects of different orientation while the latter considers only two independent damage regions (2D problems). Finally, differently from the multidirectional fixed damage models, the multidirectional damage formulation maintains during the whole damage process the coaxiality between principal directions of strains and axes of orthotropy. Hence, it keeps the motivating feature of the rotating crack models, coaxiality, which reduces stress locking, while remedying the impossibility of tracking memory of the material defects, the main objection arisen against the rotating crack concept (Bažant, 1983).

3.4 Numerical aspects of the multidirectional damage approach: smooth transition in correspondence with crack closure and re-opening

Here, the improvement of the numerical robustness of the multidirectional procedure is addressed. The passage from a damage region to the other one, performed on the base of the current principal strain directions, implies modifications of the active damage variables d^+ and d^- affecting the secant stiffness (4). Therefore, in analogy with the considerations provided in (Jefferson and Mihai, 2015), the multidirectional damage approach described in section 3.1 may suffer from convergence problems. Hindrance in achieving convergence on the residual nodal forces has been observed especially in case of load Type (ii); in fact, due to the partition adopted for this kind of loads (see Fig. 5), at load sign reversal, principal directions tend to oscillate around the boundary between a damage region and the other one.

In order to eliminate these convergence difficulties, the introduction of a transition region, of amplitude $2\theta_t$, is here proposed, with the purpose of making smoother the passage between two different damage regions.

The working principle of this smoothing procedure is explained in Fig. 7.a, where it is shown how the transition region has, as bisector, the boundary between the damage region 1 and the damage region 2. Superindices + and – for identifying the regions and their corresponding quantities r and d are dropped, since the procedure hereafter described holds for both tensile and compressive regions, provided that the principal current strain direction $\boldsymbol{p}$ refers to $\boldsymbol{p}_{max}$ and $\boldsymbol{p}_{min}$, respectively.

When the current principal strain direction $\boldsymbol{p}$ belongs to the transition region, the active damage threshold quantity r is evaluated according to Eq. (32), resorting to a hyperbolic tangent function:

$$r_t = \frac{1}{2}\left(r_1 + r_2\right) + \frac{1}{2}\left(r_1 - r_2\right) \cdot \tanh\left(\frac{2\theta_p}{\theta_t}\right) \tag{32}$$

where the pedix t stands for transition, r_1 and r_2 are the damage threshold values pertaining to region 1 and 2, respectively, and θ_p is the angle between $\boldsymbol{p}$ and the boundary. Hence, the active damage value d in the transition region is evaluated starting from the smoothed damage threshold (32) and referring to the evolution damage laws expressed in Eqs. (22).

The trend of the smoothing transition, operated on the damage threshold quantity, is plotted in Fig. 7.b, where the amplitude of the transition region is also identified. This

amplitude, defined by the parameter θ_t, is chosen to be sufficiently small compared to the rotation performed by the principal directions, which can be, at most, $\pi/2$.

In case of $\boldsymbol{p}$ falling outside the transition region, the active value of the damage variable is computed referring to r_1 or r_2, according to the procedure declared in Section 3.1.

The impact that such transition has on the numerical robustness of the multidirectional damage approach is studied in Section 5.2.3, where convergence histories for different values of the parameter θ_t are compared.

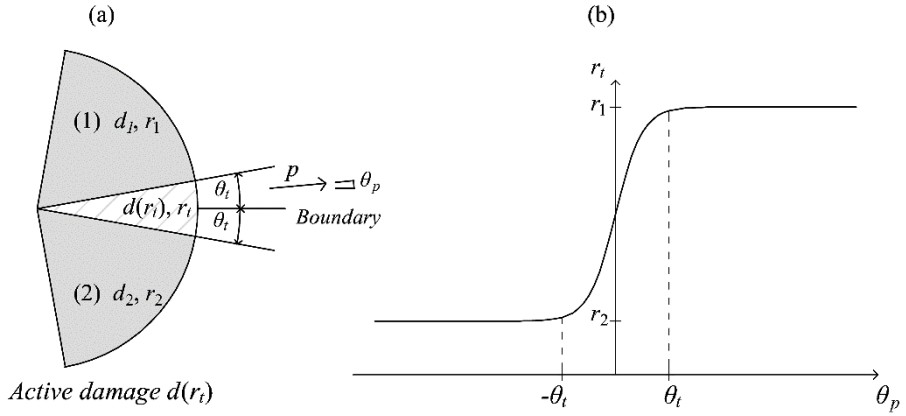

Figure 7– Smoothing of the multidirectional procedure: **(a)** identification of the transition region and **(b)** hyperbolic tangent function operating the regularization.

4. Numerical implementation of the damage model

The damage model presented in Section 2 and enriched with the multidirectional procedure described in Section 3 is implemented in a displacement-based FE code written in FORTRAN. In order to face the material non-linearity, the numerical algorithm works in an incremental-iterative way. Within a generic load increment, going from the step $n-1$ to the step n, the equilibrium global equations at each iteration i are solved using the Picard's method, based on the adoption of the global secant stiffness matrix $\boldsymbol{S}$. The solving algebraic system assumes the following form:

$$\boldsymbol{S}\left({}^{i-1}_{n}\boldsymbol{u}\right)\delta\,{}^{i}_{n}\boldsymbol{u} = -\boldsymbol{R}\left({}^{i-1}_{n}\boldsymbol{u}\right) \tag{33}$$

where $\delta\,{}^{i}_{n}\boldsymbol{u}$ is the iterative displacement vector correction adopted to compute the iterative displacement vector ${}^{i}_{n}\boldsymbol{u}$

$${}^{i}_{n}\boldsymbol{u} = {}^{i-1}_{n}\boldsymbol{u} + \delta\,{}^{i}_{n}\boldsymbol{u} \tag{34}$$

and the residual force vector $\boldsymbol{R}$ is expressed in terms of the internal $\boldsymbol{P}$ and external $\boldsymbol{F}$ force vectors:

$$\boldsymbol{R}\left({}^{i-1}_{n}\boldsymbol{u}\right)=\boldsymbol{P}\left({}^{i-1}_{n}\boldsymbol{u}\right)-{}_{n}\boldsymbol{F}=\boldsymbol{S}\left({}^{i-1}_{n}\boldsymbol{u}\right){}^{i-1}_{n}\boldsymbol{u}-{}_{n}\boldsymbol{F} \tag{35}$$

The choice of a Picard's method has two main reasons. On the one hand, it allows taking advantage, from a computational point of view, of the symmetric constitutive stiffness operator $\boldsymbol{D_E}$ (4): in fact, a symmetric local secant matrix implies a symmetric algebraic system to be solved (Eq. (33)). On the other hand, it is addressed to avoid the computation of the consistent tangent stiffness matrix necessary for the application of the Newton Raphson method. In fact, in the case of the constitutive d^+/d^- damage model here presented, this matrix is non-symmetric and requires the evaluation of the derivative of the projection operator (7), which is not straightforward.

Regarding the numerical scheme for the derivation of the constitutive law, despite the assumption of energy-equivalence and the multidirectional treatment of damage, characterizing the new formulation, a full strain-driven formalism is maintained, in order to guarantee algorithmic efficiency. To achieve this, the updating of the permanent strain tensor $\boldsymbol{\varepsilon_p}$ is made explicitly, meaning that it is performed only once, at the end of the loading step, after the attainment of convergence. This allows to compute, within each iteration, the elastic strain tensor $\boldsymbol{\varepsilon_e}$ directly from the iterative displacements and to evaluate, on the base of it, the active damage variables d^+ and d^-, the projection operator $\boldsymbol{Q}$ (7), the active secant stiffness $\boldsymbol{D_E}$ (4) and, finally, the nominal stress tensor $\boldsymbol{\sigma}$ (10). The numerical algorithm of the $d^+/\ d^-$ multidirectional damage model is synthetized in Table 1. Three subroutines are adopted in order to make clearer the working principles of the multidirectional procedure. They are:

- *Damage multidirectional saving* ($d^{\pm}$, $r^{\pm}$, $\boldsymbol{\varepsilon_e}$; $d_{1,2}{}^{\pm}$, $r_{1,2}{}^{\pm}$): the converged d^+ (d^-) damage value is saved as $d_1{}^+$ or $d_2{}^+$ ($d_1{}^-$ or $d_2{}^-$) in a region, depending on the maximum (minimum) strain ($\boldsymbol{\varepsilon_e}$) direction which has generated it (input parameters $\boldsymbol{\varepsilon_e}$, $d^{\pm}$, $r^{\pm}$; output parameters $d_{1,2}{}^{\pm}$, $r_{1,2}{}^{\pm}$);
- *Damage multidirectional updating* ($\boldsymbol{\varepsilon_e}$, $d_{1,2}{}^{\pm}$, $r_{1,2}{}^{\pm}$, $\tau^{\pm}$; $d^{\pm}$, $\dot{d}^{\pm}$, $r^{\pm}$)*:* it provides the active damage value d^+ (d^-), its rate $\dot{d}^+$ ($\dot{d}^-$) and the active damage threshold r^+ (r^-) on the base of the current damage equivalent stress quantity τ^+ (τ^-) which is compared with the damage threshold $r_1{}^+$ or $r_2{}^+$ ($r_1{}^-$ or $r_2{}^-$) saved in the region where the principal maximum (minimum) strain ($\boldsymbol{\varepsilon_e}$) direction falls (input parameters $\boldsymbol{\varepsilon_e}$, $d_{1,2}{}^{\pm}$, $r_{1,2}{}^{\pm}$, $\tau^{\pm}$; output parameters $d^{\pm}$, $\dot{d}^{\pm}$ and $r^{\pm}$);

- *Damage regions updating:* in loading conditions, for load Type (ii), it changes the bisectors and the amplitudes of the damage regions, with reference to (30).

Load increment n:

Known quantities:

${}^{n-1}\boldsymbol{\varepsilon}$, ${}^{n-1}\boldsymbol{\varepsilon_p}$, ${}^{n-1}d_{1,2}^{\pm}$, ${}^{n-1}r_{1,2}^{\pm}$; only for load Type (ii): ${}^{n-1}r_{\theta}^{\pm}$.

Iteration i:

(i) Compute the nominal elastic strain tensor ${}^{n,i}\boldsymbol{\varepsilon_e}$: ${}^{n,i}\boldsymbol{\varepsilon_e} = {}^{n,i}\boldsymbol{\varepsilon} - {}^{n-1}\boldsymbol{\varepsilon_p}$.

(ii) Compute the projection operators ${}^{n,i}\boldsymbol{Q}$ and $\boldsymbol{I} - {}^{n,i}\boldsymbol{Q}$ by means of the spectral decomposition of the nominal strain tensor ${}^{n,i}\boldsymbol{\varepsilon_e}$ (Eqs. (6) and (7)).

(iii) Compute the elastic stress tensor ${}^{n,i}\boldsymbol{\sigma_e}$ (Eq. (13)).

(iv) Compute the equivalent stress quantities ${}^{n,i}\tau^{\pm}$ (Eqs. (16));

(v) Only for load Type (ii): compute the equivalent deviation quantity ${}^{n,i}\tau_{\theta}^{\pm}$ (Eq. (28)) on the base of ${}^{n,i}\boldsymbol{\varepsilon_e}$;

if ${}^{n,i}\tau_{\theta}^{\pm} < {}^{n-1}r_{\theta}^{\pm}$: ${}^{n,i}r_{\theta}^{\pm} = {}^{n,i}\tau_{\theta}^{\pm}$ and call "*Damage regions updating*";

if ${}^{n,i}\tau_{\theta}^{\pm} > {}^{n-1}r_{\theta}^{\pm}$: ${}^{n,i}r_{\theta}^{\pm} = {}^{n-1}r_{\theta}^{\pm}$.

(vi) Call *"Damage multidirectional updating (* ${}^{n,i}\boldsymbol{\varepsilon_e}$, ${}^{n-1}d_{1,2}^{\pm}$, ${}^{n-1}r_{1,2}^{\pm}$, ${}^{n,i}\tau^{\pm}$; ${}^{n,i}d^{\pm}$, ${}^{n,i}\dot{d}^{\pm}$, ${}^{n,i}r^{\pm}$ *)"*.

(vii) Compute the operator ${}^{n,i}\boldsymbol{A}^{*}$ (Eq. (5)):

$${}^{n,i}\boldsymbol{A}^{*} = \sqrt{1-{}^{n,i}d^{+}}\,{}^{n,i}\boldsymbol{Q} + \sqrt{1-{}^{n,i}d^{-}}\left(\boldsymbol{I} - {}^{n,i}\boldsymbol{Q}\right).$$

(viii) Compute the nominal stress ${}^{n,i}\boldsymbol{\sigma}$ (Eq. (10)): ${}^{n,i}\boldsymbol{\sigma} = {}^{n,i}\boldsymbol{A}^{*} : \boldsymbol{D_0} : {}^{n,i}\boldsymbol{A}^{*} : {}^{n,i}\boldsymbol{\varepsilon_e}$.

(ix) Check convergence:

NO convergence: go to the iteration i+1 and start again from (i).

YES convergence:

- Update: ${}^{n}\boldsymbol{\varepsilon} = {}^{n,i}\boldsymbol{\varepsilon}$; only for load Type (ii): ${}^{n}r_{\theta}^{\pm} = {}^{n,i}r_{\theta}^{\pm}$.
- Update permanent strain tensor (Eq. (12)):

$$\Delta^{n}\boldsymbol{\varepsilon_p} = \left[b^{+}\cdot H\left({}^{n,i}\dot{d}^{+}\right) + b^{-}\cdot H\left({}^{n,i}\dot{d}^{-}\right)\right]\frac{\left\langle {}^{n,i}\boldsymbol{\sigma_e} : \left({}^{n}\boldsymbol{\varepsilon} - {}^{n-1}\boldsymbol{\varepsilon}\right)\right\rangle}{{}^{n,i}\boldsymbol{\sigma_e} : {}^{n,i}\boldsymbol{\varepsilon_e}}\cdot {}^{n,i}\boldsymbol{\varepsilon_e}$$

$${}^{n}\boldsymbol{\varepsilon_p} = {}^{n-1}\boldsymbol{\varepsilon_p} + \Delta^{n}\boldsymbol{\varepsilon_p}.$$

- For load Type (i): call "*Damage multidirectional saving (* ${}^{n,i}d^{\pm}$, ${}^{n,i}r^{\pm}$, ${}^{n,i}\boldsymbol{\varepsilon_e}$; ${}^{n}d_{1,2}^{\pm}$, ${}^{n}r_{1,2}^{\pm}$ *)*".
- For load Type (ii)

  if ${}^{n}r_{\theta}^{\pm} < \cos(\theta_{min})$: call "*Damage multidirectional saving (* ${}^{n,i}d^{\pm}$, ${}^{n,i}r^{\pm}$, ${}^{n,i}\boldsymbol{\varepsilon_e}$; ${}^{n}d_{1,2}^{\pm}$, ${}^{n}r_{1,2}^{\pm}$ *)*";

  if ${}^{n}r_{\theta}^{\pm} = \cos(\theta_{min})$: ${}^{n}d_{1,2}^{+} = {}^{n,i}d^{+}$; ${}^{n}d_{1,2}^{-} = {}^{n,i}d^{-}$; ${}^{n}r_{1,2}^{+} = {}^{n,i}r^{+}$; ${}^{n}r_{1,2}^{-} = {}^{n,i}r^{-}$.
- Go to the next increment load n+1.

Table 1 – Numerical algorithm of the constitutive law for the multidirectional damage model.

5. Validation examples

In this section, the energy-equivalent damage model described in Section 2 and the multidirectional procedure specifically thought for cyclic loadings (Section 3) are validated by means of comparisons between experimental and numerical results, considering 2D plane stress problems. In Section 5.1, three examples involving unreinforced concrete structural elements are solved, in order to investigate the adequacy of the new d^+/d^- damage model, specifically the effects produced by the adoption of the constitutive secant stiffness operator (4), derived within an energy-equivalence framework. For these purposes, only monotonically increasing loadings are analysed. Conversely, in Section 5.2, the potentialities of the multidirectional damage procedure described in Section 3 are shown with reference to a masonry wall and a reinforced concrete wall, both subjected to cyclic shear conditions. Finally, the efficiency of the smooth transition proposed in Section 3.4 for crack closure and reopening is discussed.

In all the analyses, the numerical algorithm detailed in Table 1 is adopted. Specifically, the convergence in a time step n is attained when both the ratio between the norm of the iterative residual forces $\boldsymbol{R}$ and the external forces $\boldsymbol{F}$ (see Eq. (35)) and the ratio between the norm of the iterative displacement increments $\delta\,{}^{i}_{n}\boldsymbol{u}$ and the total displacements ${}^{i}_{n}\boldsymbol{u}$ (see Eq. (34)) are lower than 1%.

Depending on the example of application, triangular (3-nodes) and/or quadrilateral (4-node) elements are adopted in the discretization. The crack width parameter l_{dis}, introduced in the evolution damage law (22.b) for guaranteeing mesh-size objectivity of the results, is computed according to the area A_e of the finite element: for triangles, $l^2_{dis} = 4/\sqrt{3}\,A_e$ for quadrilateral elements, $l^2_{dis} = A_e$.

5.1 Monotonic loadings: validation of the energy-equivalent d^+/d^- damage model

Three different structural applications are studied with the energy-equivalent d^+/d^- damage model: a wedge-splitting test performed on a concrete specimen in the experimental program described in (Trunk, 2000), a three-point bending test shown in (Kormeling and Reinhardt, 1983) and a mixed-mode three-point bending test documented in (Gálvez et al., 1998), both on single-edged-notched concrete beams. The geometry, the boundary and the loading conditions for the just mentioned examples are illustrated in Fig. 8, Fig. 9 and Fig. 10, respectively.

In all the problems, the increasing forces P are applied by imposing increasing displacements of the application points.

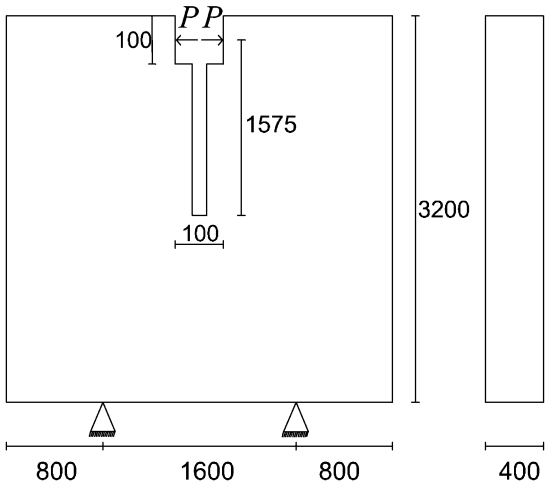

Figure 8 – Wedge-splitting test set-up.

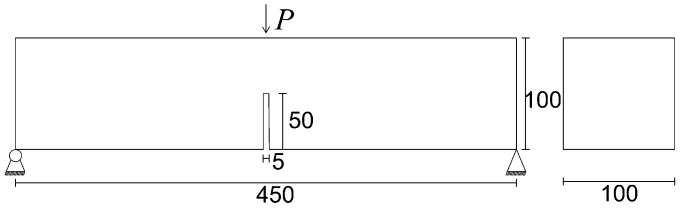

Figure 9 – Three-point bending test set-up.

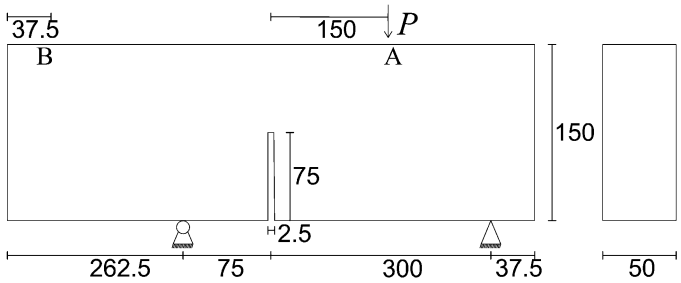

Figure 10 – Mixed mode three-point bending test set-up.

The mechanical properties assumed for concrete in each case are summarized in Table 2, Table 3 and Table 4, respectively.

E [MPa]	ν [-]	f^+ [MPa]	f^- [MPa]	γ_e^- [-]	γ_p^- [-]	G_f^+ [N/mm]	G_f^- [N/mm]	$b+$ [-]	b^- [-]	f_b^-/f^- [-]
28300	0.2	1.59	-25	0.33	1.33	0.35	35	0.05	0.3	1.16

Table 2 – Constitutive parameters of concrete for the wedge-splitting test.

E [MPa]	ν [-]	f^+ [MPa]	f^- [MPa]	γ_e^- [-]	γ_p^- [-]	G_f^+ [N/mm]	G_f^- [N/mm]	$b+$ [-]	b^- [-]	f_b^-/f^- [-]
20000	0.2	2.4	-24	0.33	1.33	0.133	30	0.05	0.3	1.16

Table 3 – Constitutive parameters of concrete for the three-point bending test.

E [MPa]	ν [-]	f^+ [MPa]	f^- [MPa]	γ_e^- [-]	γ_p^- [-]	G_f^+ [N/mm]	G_f^- [N/mm]	$b+$ [-]	b^- [-]	f_b^-/f^- [-]
38000	0.2	3	-54	0.33	1.33	0.069	38	0.05	0.3	1.16

Table 4 – Constitutive parameters of concrete for the mixed-mode three-point bending test.

The mesh has been generated taking care of refining the discretization where the propagation of the crack is expected; for the wedge-splitting test, a mesh of 3353 quadrilateral elements is adopted with a representative length in the proximity of the cracking zone equal to 17.5 mm. In the three-point bending and in the three-point mixed-mode bending tests, the concrete beams are discretized with 2752 and 13336 elements, respectively: in the regions around the notch, triangular elements with an average size of 2.5 mm are used while the other zones are discretized with larger quadrilateral meshes.

The adequacy of the proposed orthotropic d^+/d^- damage model in capturing the nonlinear behaviour is proven by comparing the numerical and the experimental results in terms of deformed configurations, damage distribution, applied load P – crack mouth opening displacement $CMOD$ and/or applied load P – displacement of relevant points.

Regarding the wedge-splitting test, as expected due to the problem symmetry, the localization of the tensile damage occurs in correspondence of the notched zone (see Fig. 11.a and Fig. 11.b) and is vertical, in accordance with the vertical crack path found experimentally. The numerical P - $CMOD$ curve is compared in Fig. 12 with the experimental one: both the peak-load and the post-peak behaviour are satisfactorily described with the proposed model.

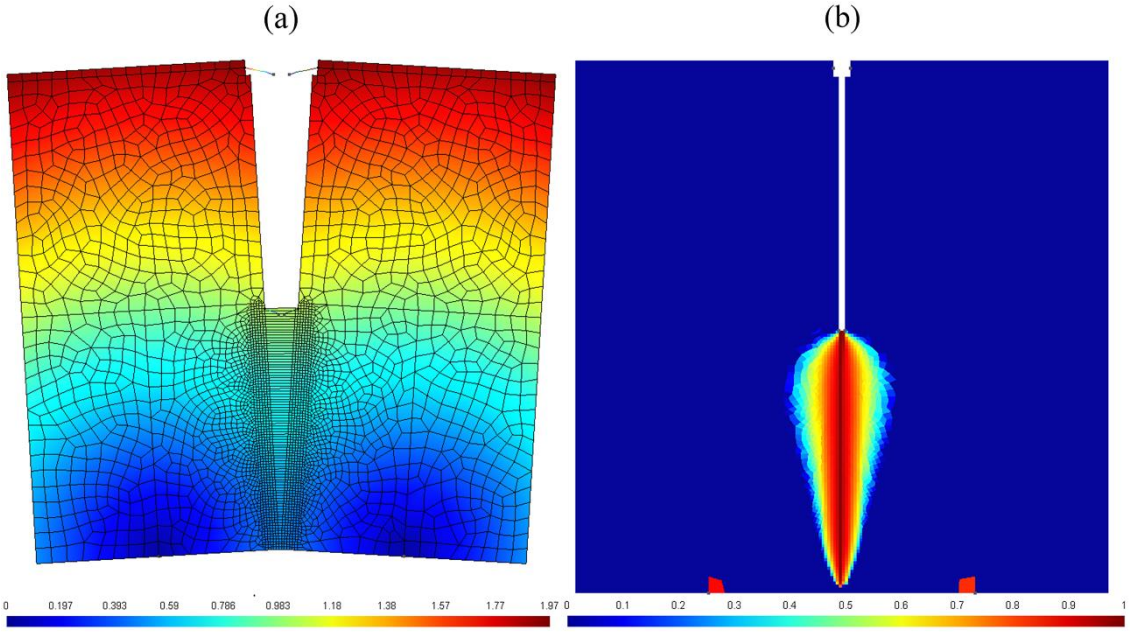

Figure 11 – Wedge-splitting test: **(a)** deformed configuration (× 100) (in mm)and **(b)** tensile damage distribution.

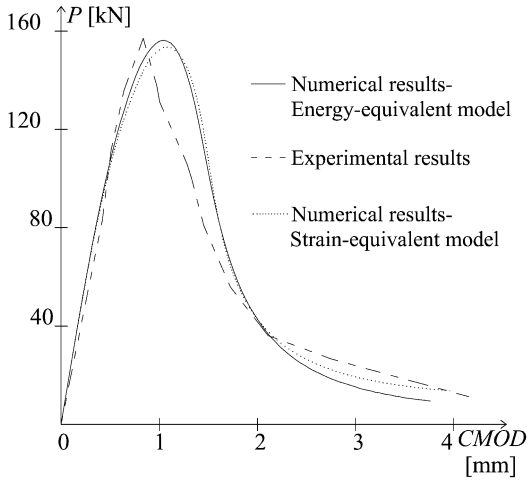

Figure 12 – Load P – $CMOD$ curve for the wedge-splitting test: comparison between numerical and experimental results.

The accordance of the results obtained numerically with the experimental ones is evident also for the three point bending test, as confirmed by the deformed configuration of the beam and by the d^+ distribution (Fig. 13.a and Fig. 13.b), which show the localization of the maximum deformations in correspondence of the mid-span, above the notch. The agreement between experimental and numerical results is evident also in Fig. 14, where the load P – mid-point displacement δ curve obtained with the proposed damage model falls in between the maximum and minimum experimental envelopes.

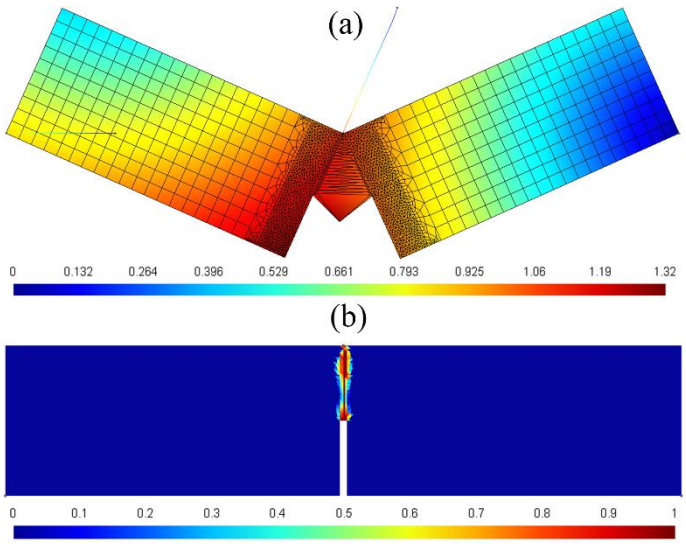

Figure 13 – Three-point bending test: **(a)** deformed configuration (× 100) (in mm) and **(b)** tensile damage distribution map.

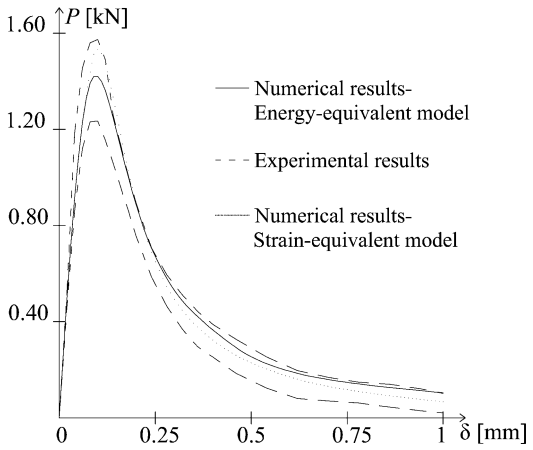

Figure 14 – Load $P - \delta$ curve for the three-point bending test: comparison between numerical and experimental results.

Finally, as regards the three-point mixed-mode bending test, the deformed configuration (Fig. 15.a) and the distribution of the tensile damage (Fig. 15.b) are in perfect agreement with the crack trajectory found in the experiment, which has an inclined direction of propagation, as accurately documented in (Gálvez et al., 1998). The structural curves obtained with the proposed orthotropic model, in terms of applied load P – *CMOD* (Fig. 16.a) and applied load P – displacement of point B (Fig. 16.b), fit satisfactorily with the experimental results, except for a slight overestimation of the dissipated energy in the post peak regime.

All the problems just described are solved also with the constitutive law presented in (Faria et al., 1998), derived in the framework of strain-equivalence, but resorting to the same permanent strain rate (12), damage criterion Eqs. (16) and damage evolution laws (22) here considered. The corresponding numerical curves are plotted in Fig. 12, Fig. 14 and Fig. 16 together with the experimental ones and the ones obtained with the d^+/d^- damage model of Section 2.

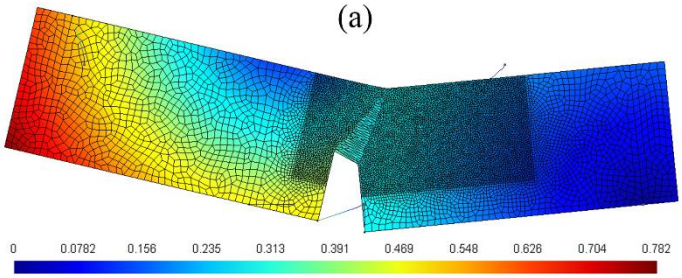

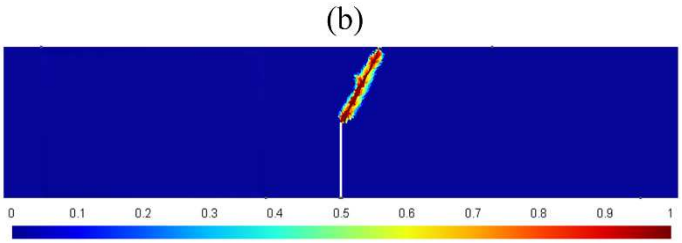

Figure 15 – Three-point mixed-mode bending test: **(a)** deformed configuration (in mm) (× 100) and **(b)** tensile damage distribution map.

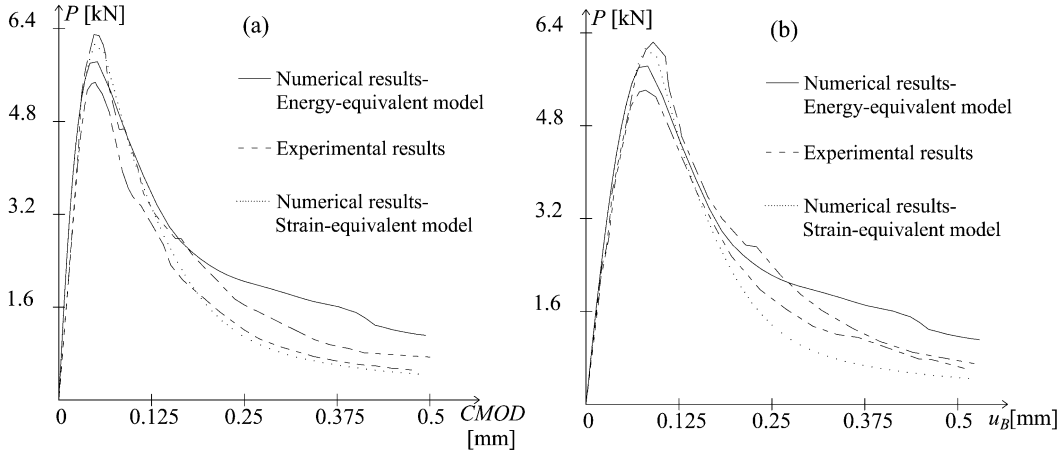

Figure 16 – **(a)** Load $P - CMOD$ curve and **(b)** load $P - u_B$ curve for the three-point mixed-mode bending test: comparison between numerical and experimental results.

The objective is to discuss the effects of the energy-equivalence assumption, here adopted for the derivation of the constitutive law (10), compared with the strain-equivalence hypothesis. In all cases, it is possible to note how the differences between the two different formulations are substantially slight, being both of them able to reproduce satisfactorily the laboratory results. Hence, although the choice of energy-equivalence ensures a gain in thermodynamic consistency with respect to the strain-equivalence one, as observed in (Cervera and Tesei, 2017), both the formulations are adequate in describing the strain-softening response typical of quasi-brittle materials.

5.2 Cyclic loadings: validation of the multidirectional d^+/d^- damage model

5.2.1 Masonry shear panel under cyclic conditions

The first problem analyzed with the model presented in Section 2 enriched with the multidirectional procedure described in Section 3 is an unreinforced brick masonry wall under in-plane quasi-static shear loading conditions. The reference solution is represented by the results of laboratory tests provided in (Anthoine et al., 1994) and (Magenes and Calvi, 1997), dealing with a laboratory campaign addressed to investigate the seismic

behavior of masonry existing buildings. The loading conditions of the analyzed problem are representative of the ones sustained by vertical structural elements during a seismic event, i.e. permanent vertical loads and double bending moments.

According to the experimental set-up (Anthoine et al., 1994), the wall, with an height *H*-width ratio equal to 1.35, width *B* 1000 mm and thickness 250 mm, is first subjected to a vertical compressive force of 150 kN (p = 0.6 N/mm^2) and then to cyclic horizontal displacements u_h of increasing amplitudes applied on the top boundary. The base of the panel is completely constrained and the vertical displacements of its top side are prevented, forcing the bottom and top panel sections to remain parallel. Both the geometry and the loading conditions adopted in the numerical analyses are summarized in Fig. 17.

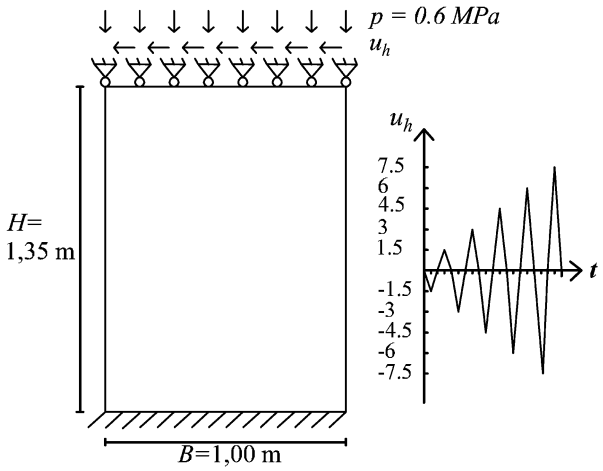

Figure 17 – Geometry, boundary and loading conditions for the masonsry shear wall.

Regarding the mechanical parameters, except for the Young's modulus and the compressive uniaxial strengths f^-, inferable from (Anthoine et al., 1994), the majority of the other values have been chosen in accordance with the experimental data expressed in (Berto et al., 2002; Magenes and Calvi, 1992) for brick masonry panels with mechanical features comparable with the ones of the analyzed wall and belonging to the same research program. The input values for the constitutive parameters adopted in the numerical simulations are collected in Table 5.

E [MPa]	ν [-]	f^+ [MPa]	f^- [MPa]	γ_e^- [-]	γ_p^- [-]	G_f^+ [N/mm]	G_f^- [N/mm]	$b+$ [-]	b^- [-]	f_b^-/f^- [-]
1500	0.15	0.26	-6.2	0.5	1.5	0.25	28	0.1	0.3	1.15

Table 5 – Constitutive parameters for the masonry panel under cyclic shear.

Due to the presence of a non-negligible constant vertical force in addition to the cyclic actions, the problem is solved by resorting to the multidirectional procedure specifically devised for load Type (ii) (Section 3.1.2), i.e. taking into account the evolution of the

damage regions related to the continuous rotation of the principal directions. The two additional deviation parameters required by the multidirectional damage procedure, θ_{min} (Eq. (29)) and θ_t (Eq. (32)), are assumed equal to $\pi/8$ and $\pi/36$, respectively.

The response of the panel obtained in the laboratory test is plotted in Fig. 18.a, in terms of the horizontal shear force F_h recorded at the top side versus the imposed horizontal displacement u_h. The curve is typical of a brittle failure mechanism dominated by shear, where the peak load, equal to 84 kN in correspondence of a drift of 0.20 %, corresponds to the formation of diagonal cracks in the center of the panel; the pre-cracking behavior is characterized by a modest hysteresis behavior while, after the attainment of the maximum carrying capacity, rapid strength and stiffness degradation and high energy dissipation are visible. The cyclic conditions are responsible for a trapezoidal cracking pattern which presents two sets of intersecting cracks in the mid-height of the panel, as well as horizontal flexural ones in correspondence of the corners.

The F_h - u_h curves obtained by the application of the multidirectional damage model, considering three quadrilateral mesh configurations with different refinement, are shown in Fig. 18.b, 18.c and 18.d. For comparison purposes, each numerical curve is plotted together with the envelope of the experimental one.

Analyzing these figures, it is evident how the dependence of the results on the discretization, ensured by the presence of the length l_{dis} in the definition of the softening moduli in tension and compression (Eq. (25)), is very small and can be considered negligible. In addition, it can be noticed that the numerical results reproduce satisfactorily the overall structural response of the shear panel: both the peak load, achieved at a drift of 0.22 % ($u_h = -3$ mm) and equal to 84,8 kN (curve in Fig. 18.d), and the post-peak softening trend are well approximated. Moreover, the effect of the multidirectional procedure is visible in the similarity of the response in terms of ultimate load, ultimate displacement and softening behaviour between positive and negative displacements. This is simulated thanks to the stiffness recovery capabilities of the multidirectional model in correspondence of loading reversal; in fact, going from negative to positive displacements, an increase in stiffness is visible in the numerical response, particularly evident in the unloading stage after the attainment of the maximum carrying capacity (cycle 2, amplitude 3mm): here, the closure of a set of diagonal cracks just opened translates in almost the total recovery of the initial stiffness, since the generation of the diagonal cracks in the orthogonal direction is not occurred yet. In the subsequent cycles,

this phenomenon, although present, is less evident because the closure of a set of cracks coincides with the re-activation of the other set of cracks previously originated.

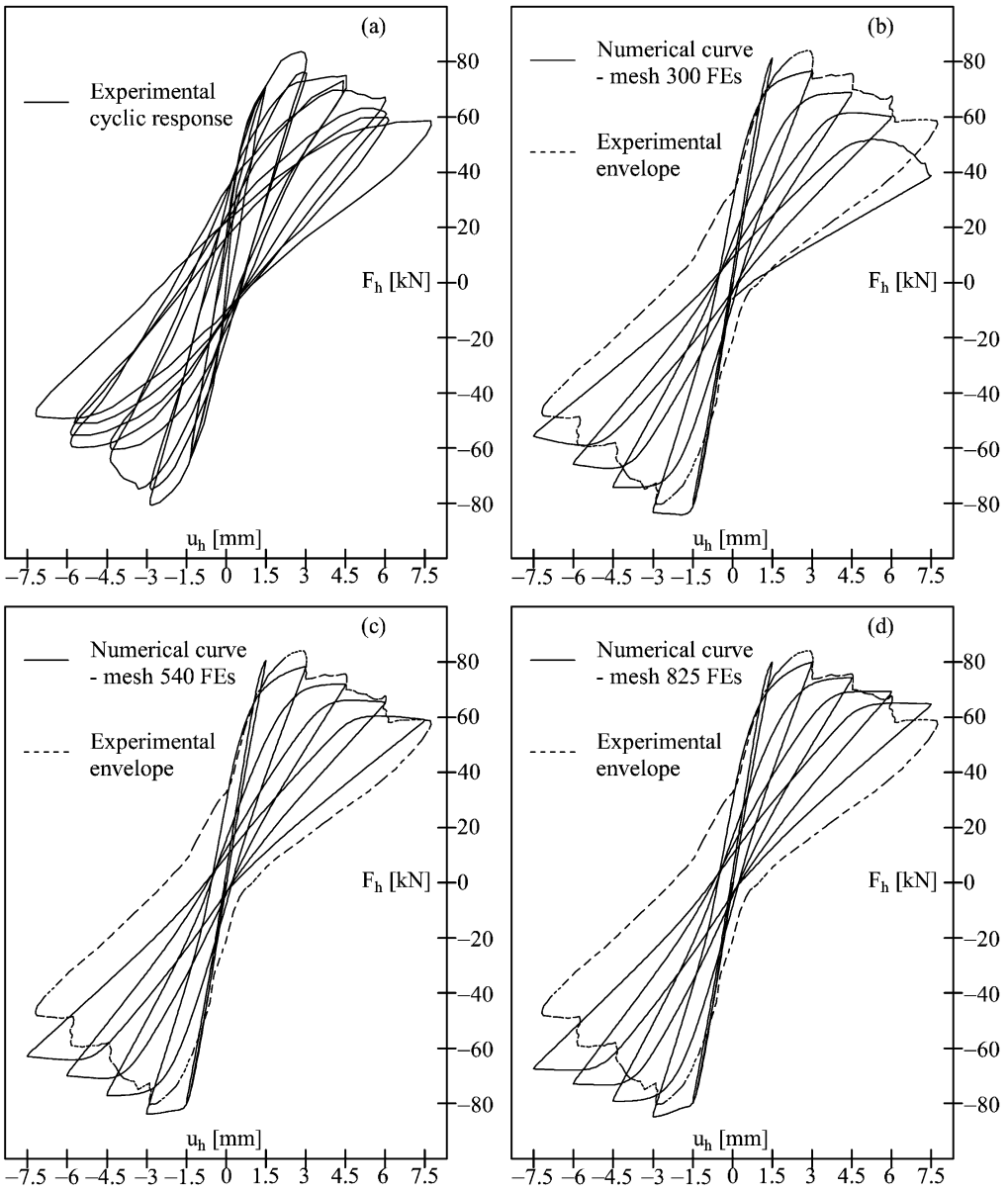

Figure 18 – Masonry wall under in-plane cyclic shear: **(a)** experimental results; **(b)**, **(c)** and **(d)** numerical results obtained with the multidirectional procedure for different mesh refinments.

To make clearer how this stiffness regain is simulated, the contour plots of the active tensile damage value d^+ corresponding to different stages of cycle 2 are shown in Fig. 19. In Fig. 19.a, 19.b and 19.c, the contour plots refer to the situations of maximum loading (u_{hmax}= −3 mm), loading reversal (u_{hmax}= +0.12 mm) and maximum reloading (u_{hminx}= +3 mm). In Fig. 19.a, the high values of damage at the center of the panel and at the two corners identify the formation of the shear and flexural cracks, respectively, induced by a horizontal displacement towards the right. Just after loading reversal, in Fig. 19.b, the closure of the previously generated cracks is represented by making inactive

the damage values displayed in Fig. 19.a: in fact, due to the rotation of the principal directions, the transition from a damage region to the other one has occurred and the active damage values coincide with the maximum ones attained during the reloading in cycle 1. Starting from this damage configuration, due to the increase of the horizontal displacement towards the left, the active damage distribution in Fig. 19.c is obtained, almost symmetric with respect to the one in Fig. 19.a.

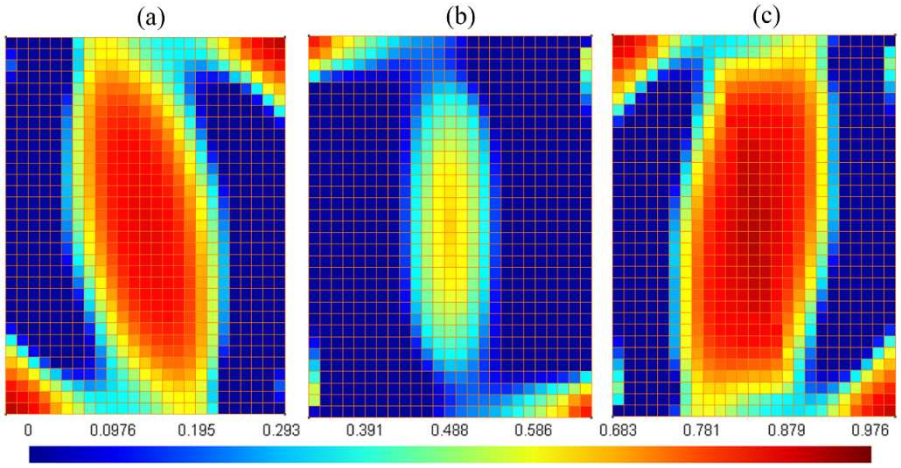

Figure 19: Active d^+ contour plots in cycle 2: **(a)** u_h=−3mm, **(b)** u_h=+0.12mm and **(c)** u_h=+3mm.

A further confirmation that the collapse mechanism captured by the numerical analysis is governed by shear is given in Fig. 20 and Fig. 21, where the maximum tensile strains ε_{max} are displayed in cycle 2 and in cycle 5, respectively, at the end of loading and at the end of the reloading stages.

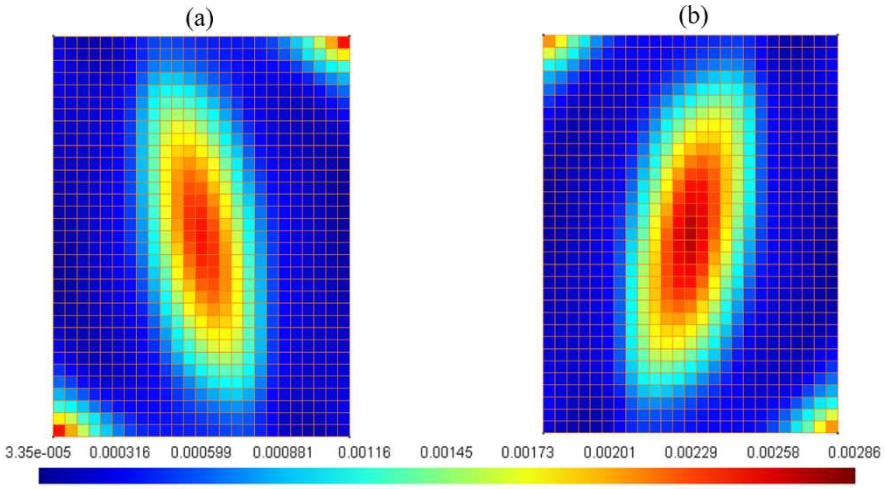

Figure 20: Maximum tensile strain contour plots in cycle 2: **(a)** u_h= −3 mm and **(b)** u_h= +3 mm.

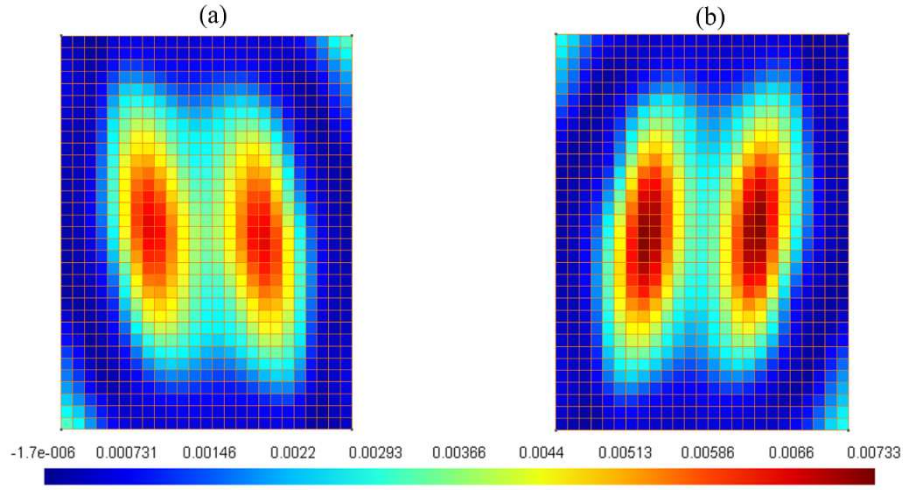

Figure 21: Maximum tensile strain contour plots in cycle 5: **(a)** u_h= −7.5 mm and **(b)** u_h= +7.5 mm.

The contour plots in Fig. 20 confirm the formation of the dominant cracking mechanism in the center of the panel; in Fig. 21, the results refer to the end of the analysis, when the crack propagation towards the corners has occurred, causing the maximum strain values to leave the central part. Although the adoption of a smeared approach does not allow identifying with accuracy the strain localization, the results shown in Fig. 20 and Fig. 21 are in good agreement with the cracking pattern observed in laboratory and documented in (Anthoine et al., 1994).

For comparison purposes, the F_h - u_h curve obtained by the adoption of the damage model without a multidirectional treatment of damage is shown in Fig. 22.a. Even though the peak load and the envelope of the experimental curve are basically captured, the lack of unilateral effects reflects in a relevant underestimation of the dissipated energy. This can be noticed both in the unrealistic shape of the hysteretic cycles and in the evolution of permanent deformations, which accumulate mainly in the positive loading stages, and not in reloading ones (in accordance with the observations provided in Section 3.2). Differently, in the response obtained with the multidirectional damage model (see Fig. 18.d), although the permanent strains are a little underestimated, their evolution is qualitatively correct, meaning that permanent deformations are generated both in the loading and in the reloading stages. In order to provide a quantitative proof of the beneficial role of the multidirectional damage approach in terms of representation of the dissipative behavior, the equivalent viscous damping coefficients are computed for each load cycle, referring to the numerical response with and without enhanced MCR capabilities, Fig. 18.d and Fig. 22.a, respectively. The equivalent viscous damping is

evaluated as the ratio between the energy dissipated in a cycle W_d and the elastic energy W_e at the maximum displacement u_{hmax}:

$$\xi_{eq} = \frac{W_d}{2\pi\left(W_e^+ + W_e^-\right)} \tag{36}$$

In Fig. 22.b, these quantities are plotted as a function of the drift (u_{hmax}/H) and compared with the ones derived from the experimental response (data provided by Magenes and Calvi (1997)). On the one hand, Fig. 22.b shows the adequacy of the multidirectional model in treating the cyclic shear failure: after cracking, the numerical trend of the equivalent viscous damping is close to the experimental one, meaning that the growth of the dissipated energy due to increasing damage and increasing displacement demand is well reproduced. The slight lower values obtained in the analyses can be attributed to the slight underestimation of the permanent strains. On the other hand, Fig. 22.b confirms the incapability of a pure scalar damage formulation in describing the real dissipative behavior under shear cyclic conditions, because independent degradation processes along different directions can not be represented.

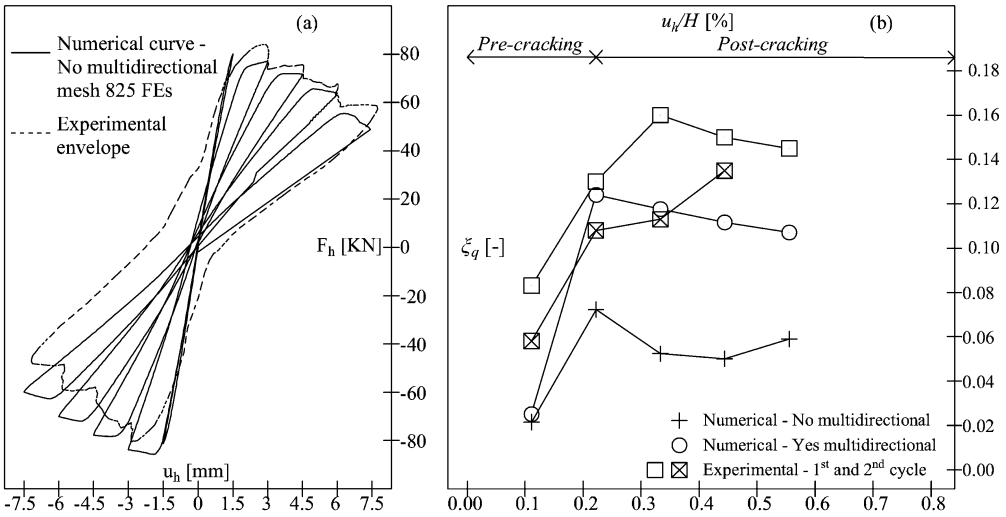

Figure 22 – Masonry shear wall under in-plane cyclic shear: **(a)** numerical results without the multidirectional procedure; **(b)** comparison in term of viscous damping coefficients between the numerical response obtained with and without the multidirectional procedure.

As mentioned above, a slight underestimation of the permanent deformations is visible in the numerical response from Fig. 18.d. This deserves some further consideration on the adequacy of the simplified definition (12) here adopted for the irreversible strain tensor $\boldsymbol{\varepsilon_p}$ and the importance of this model component in cyclic loading conditions. To do this, two additional analyses are carried out, varying the values of the material parameters b^+ and b^- with respect to the ones indicated in Table 5. Specifically, both the case of high

permanent deformations ($b^+ = 0.17$ and $b^- = 0.45$) and null permanent deformations ($b^+ = 0$ and $b^- = 0$) are considered. The resulting F_h - u_h curves, obtained using the finer mesh, are plotted in Fig. 23. Moreover, these solutions are also re-elaborated in terms of damping coefficients-drift trends in Fig. 24, in order to directly evaluate the variation of energy dissipation associated to the variation of ε_p.

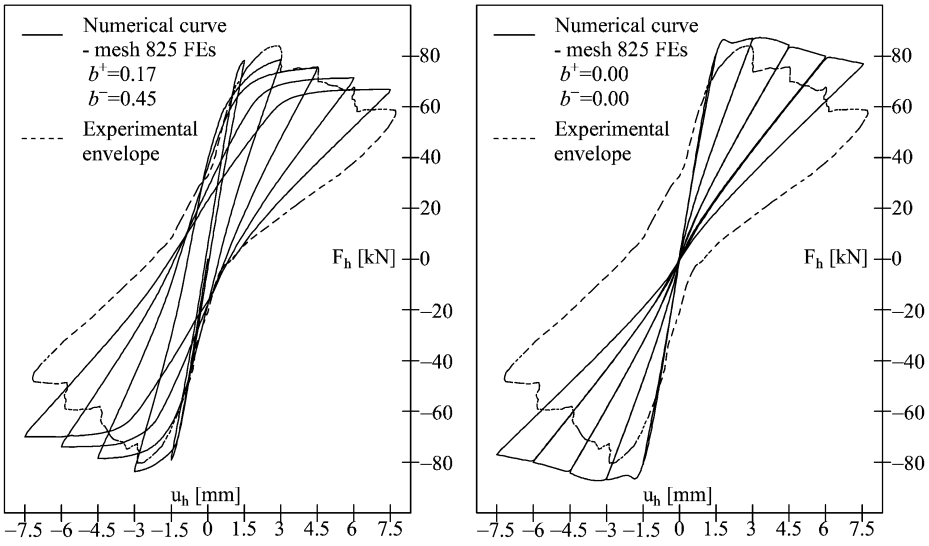

Figure 23 – Masonry shear wall under in-plane cyclic shear: F_h - u_h curves in case of **(a)** high permanent deformations and **(b)** absent permanent deformations.

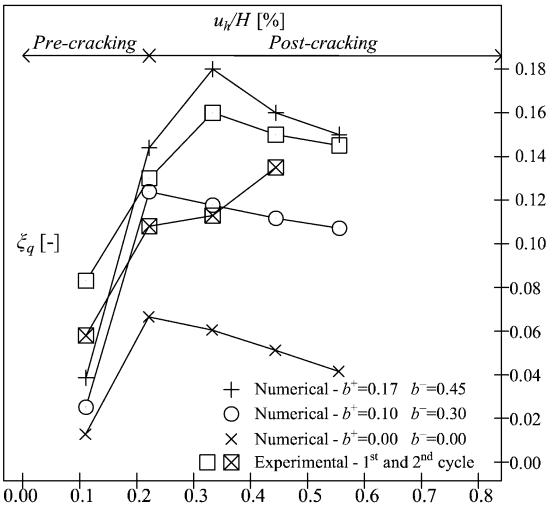

Figure 24 – Masonry shear wall under in-plane cyclic shear: numerical responses with different levels of permanent deformations compared in terms of viscous damping coefficients.

Some relevant aspects emerge from the analysis of these figures. Firstly, although the inclusion of permanent deformations in the damage model is perfomed in a simplified manner, it results adequate for describing the experimental evidence, both in terms of residual deformations at complete unloading (Fig. 23.a) and in terms of energy dissipation capacity (Fig. 24). Secondly, a less pronounced softening response is obtained when the

permanent deformations are not included (Fig. 23.b); this is not surprising because, according to the coupled definition (25) of the softening modulus, a reduction of the permanent deformations implies a reduction of the softening modulus, hence a slower increase of damage. Moreover, the unrealistically low values of ξ_{eq} obtained with null $\boldsymbol{\varepsilon_p}$ (Fig. 24) are very similar to the ones derived without the multidirectional procedure, in case of $b^+ = 0.1$ and $b^- = 0.3$ (Fig. 22.b). It is concluded that the modelling of permanent deformations is important as the modelling of microcrack closure-reopening effects for a correct representation of the behaviour of quasi-britttle structures under cyclic loading.

5.2.2 RC wall under cyclic shear

The second problem studied with the multidirectional procedure described in Section 3 is a reinforced concrete wall subjected to horizontal cyclic shear forces, tested within the French national research project CEOS.fr (Rospars and Chauvel, 2014). The specimen analyzed is the one identified in the experimental campaign with the acronym SHW2 and represents a 1/3 reduced-scale model of reinforced concrete thick shear walls employed in industrial buildings to resist seismic loadings.

In the numerical analysis, the experimental set-up, detailed in (Rospars and Chauvel, 2014; Bisch et al., 2014), is reproduced as shown in Fig. 25: the reinforced concrete specimen (Zone 1, 2), of overall dimensions 4.2 m × 1.05 m × 0.15 m, is connected on the top and on the bottom to highly reinforced thick horizontal beams (Zone 3 and Zone 4), which allow redistributing the shear loading on the panel. The horizontal action, in the laboratory test assigned by means of hydraulic actuators placed on each side of the top beam, 100 mm over the wall, is provided in terms of horizontal imposed displacements u_h alternated on the Surfaces 1 and 2.

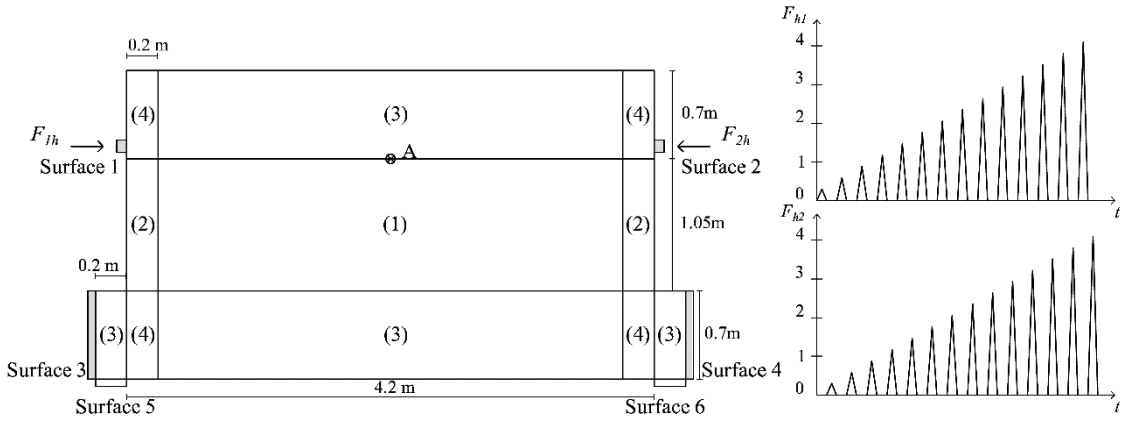

Figure 25 – Geometry, boundary and loading conditions for the masonsry shear wall.

Moreover, the constraint represented by the steel frame in which the whole test body is installed, is modelled by preventing horizontal displacements on Surfaces 3 and 4 and vertical displacements on Surfaces 5 and 6.

Rebars ϕ 10, spaced 100 mm in both vertical and horizontal directions on both faces of the wall (Zone 1) are considered while vertical rebars ϕ 25 and ϕ 32 are added in the left and right sides of the wall (Zone 2), in order to control the opening of cracks due to bending.

In the highly reinforced zones, specifically the top and bottom beams (Zone 3, 4) and the left and right parts of the wall (Zone 2), it is assumed that the concrete behaviour is elastic. Hence, the damage formulation developed in Section 2 and Section 3 is applied only to Zone 1. The mechanical parameters adopted for concrete, belonging to the class C40, are collected in Table 6. They have been chosen in accordance to (Rospars and Chauvel, 2014; Vassaux et al., 2015) and, in absence of data availability, calibrated in order to optimize the fitting between numerical and experimental results.

E [MPa]	ν [-]	f^+ [MPa]	f^- [MPa]	γ_e^- [-]	γ_p^- [-]	G_f^+ [N/mm]	G_f^- [N/mm]	$b+$ [-]	b^- [-]	f_b^-/f^- [-]
22000	0.2	3.9	-42	0.4	1.6	0.7	45	0.1	0.35	1.16

Table 6 – Constitutive parameters for the problem of the RC wall under cyclic shear.

The reinforcement is modeled as follows, exploiting the fact that it is oriented along the Cartesian directions x and y. Assuming the hypothesis of perfect adherence between concrete and rebars, the axial forces sustained by steel in the horizontal and vertical direction, P_{sx} and P_{sy}, are computed starting from the deformations ε_x and ε_y in the concrete, taking into account the percentage of horizontal and vertical reinforcement ρ_x and ρ_y. The uniaxial constitutive law chosen to represent the cyclic behavior of the reinforcement is the one proposed in (Menegotto and Pinto, 1973) and illustrated in Fig. 26. The expression for the steel stress σ_s is explicited in (Faria et al., 2004).

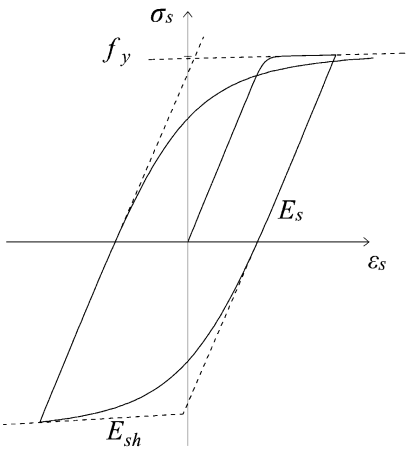

Figure 26 – Constitutive law of the reiforcement under unixial cyclic loading history.

The parameters adopted in the analyses for the characterization of the reinforcement are the following: Young's elastic modulus E_s = 210000 MPa, hardening modulus E_{sh} = 2100 MPa, yielding stress f_y = 420 MPa and three constants suitably chosen to fit the Bauschinger effect observed experimentally a_1 = 18.5, a_2 = 0.15 and a_3 = 20. The percentages of steel reinforcement considered in the different Zones highlighted in Fig. 25 are summarized in Table 7, together with the thickness of each Zone.

	ρ_x [-]	ρ_y [-]	Thickness [mm]
Zone 1	0.011	0.011	150
Zone 2	0.025	0.243	150
Zone 3	0.043	0.005	450
Zone 4	0.048	0.155	450

Table 7 – Percentage of the reinforcement and thickness for each Zone of the RC shear wall's body test.

Due to the absence of vertical loads, except for the self-weight which is negligible compared to the horizontal cyclic action, the multidirectional approach is applied referring to load Type (i), considering non-evolving damage regions during the loading history (Section 3.1.1).

In Fig. 27, the experimental results in terms of global horizontal force F_h – horizontal displacement u_{hA} of point A on the top side of the specimen (see Fig. 25) are plotted (Bisch et al., 2014). In Fig. 28, four different numerical predictions are shown: Fig. 28.a and Fig. 28.b exhibit the force-displacement curves obtained by means of the multidirectional procedure, considering two different quadrilateral mesh refinements; Fig. 28.c represents the numerical response derived by applying the formulation of Section 2 without a multidirectional treatment of damage; finally, in Fig. 28.d the results are obtained with the multidirectional procedure and increasing the intensity of the

permanent deformations with respect to the values presented in Table 6 (b^+= 0.18 and b^-= 0.45).

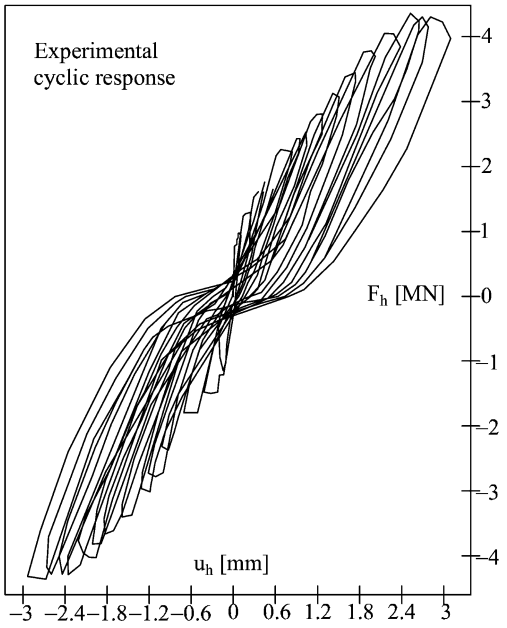

Figure 27 – RC wall under in-plane cyclic shear: experimental results.

First of all, comparing Fig. 28.a and Fig. 28.b, a very low dependence of the results from the discretization can be appreciated. Secondly, good representativeness of the experimental curve is noticed. Specifically, the progressive evolution of degradation with the development of cracking is caught, as well as the lateral resistance of the structure (4.07 MN against 4.3 MN). Even in terms of displacement capacity, the numerical and observed results are in agreement: the slightly greater deformability visible in Fig. 27 for high load cycles is attributable to the assumption of elastic behavior for the Zones 2, 3 and 4 displayed in Fig. 25. In addition, comparing Fig. 28.b and Fig. 28 d, it is worth noting that the level of permanent deformations experimentally observed is better modelled by increasing the parameters b^+ and b^-. This represents a further confirmation of the adequacy of Eq. (12) for describing the evolution of $\boldsymbol{\varepsilon_p}$.

For what concern the effects of the alternating loadings, the global response obtained with the adoption of the multidirectional procedure (Fig. 28.a, Fig. 28.b and Fig. 28.d) is essentially symmetric. This proves an appropriate consideration of the microcracks closure-reopening phenomena. In fact, the same peak loads and the same dissipative trends can be obtained in the loading and reloading stages only by means of appropriate stiffness recovery capabilities upon loading reversal. These features are absent in the response obtained without the multidirectional procedure (Fig. 28.c), in which the full conservation of damage from the loading to the reloading stages is evident and is due to

the impossibility of distinguishing between two sets of defects with different orientation. In addition, as discussed in Section 3.2, the lack of unilateral capabilities have consequences even on the evolution of permanent strains, which unrealistically accumulate only for positive thrusts.

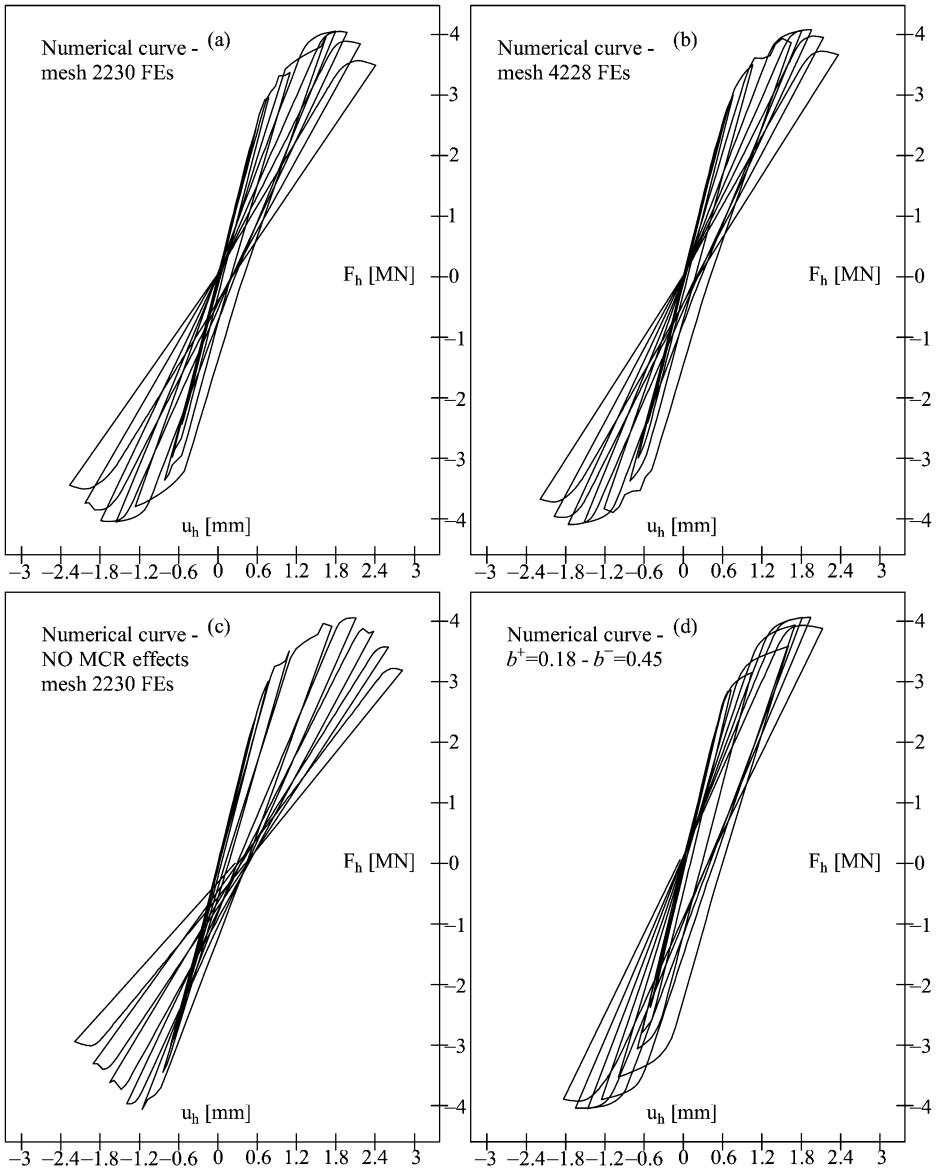

Figure 28 – RC wall under in-plane cyclic shear: **(a)** and **(b)** numerical results obtained with the multidirectional procedure for two different mesh refinments; **(c)** numerical results without the multidirectional procedure; **(d)** numerical results obtained with the multidirectional procedure and with an higher level of permanent deformations.

The only notable discrepancy between numerical and observed results lies in the pinched shape of the hysteresis cycles, which is evident in Fig. 27 and is not appreciable in Fig. 28.a, Fig. 28.b and Fig. 28.d. Pinching is associated to the bond slip between concrete and rebars (Vecchio, 1999), neglected in the analysis due to the hypothesis of perfect

adherence. Removing such an assumption would add significant complexity to the model and it is not in line with the objective of the present example of application, which is to show the enhanced unilateral capabilities of concrete ensured by the application of the multidirectional procedure.

In order to exhibit how the multidirectional approach allows reproducing the stiffness recovery, the contour plots of the active tensile damage at the end of the loading (u_{hA} = 1.55 mm) and at the end of the reloading (u_{hA} = −1.35 mm) in the fourth cycle of the curve plotted in Fig. 28.b are displayed in Fig. 29.a and Fig. 29.b, respectively. The approach is based on the deactivation of some values of damage (the one referred to the closed cracks) and on the reactivation of other values (the one referred to the open ones).

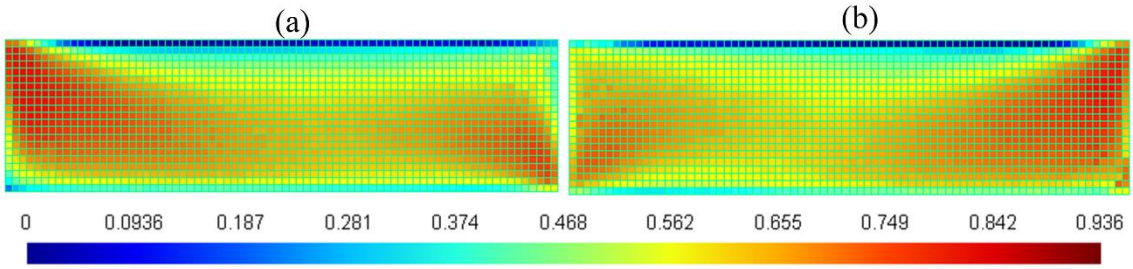

Figure 29 – Contour plots of the active tensile damage value $d^+$for the RC wall under in-plane cyclic shear: **(a)** u_{hA} = 1.55 mm and **(b)** u_{hA} = −1.35 mm.

Finally, the symmetry found in the active damage contour plots (Fig. 29) between the two sets of alternating active cracks reflects in a symmetric distribution of the longitudinal strains ε_{xx}, between the situation u_{hA} = 2.35 mm and u_{hA} = −2.2 mm, as shown in Fig. 30.a and Fig. 30.b respectively. These contour plots reproduce satisfactorily the two symmetric sets of cracks observed in the laboratory test (Rospars and Chauvel, 2014) and confirm the adequacy of the proposed mechanical model in dealing with cyclic shear actions.

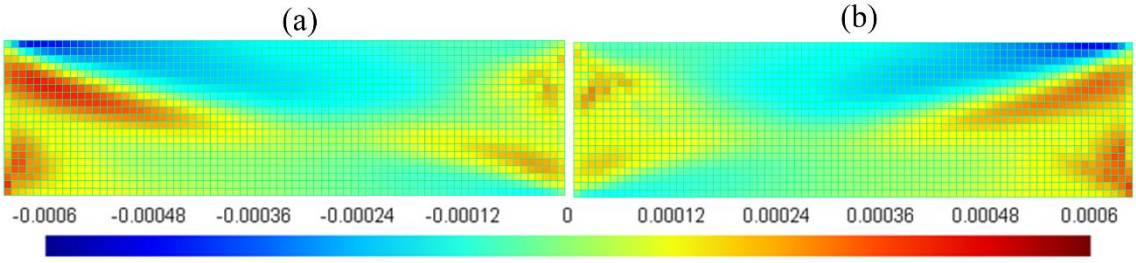

Figure 30 – Contour plots of the longitudinal strains ε_{xx} for the RC wall under in-plane cyclic shear: **(a)** u_{hA} = 2.35 mm and **(b)** u_{hA} = −2.2 mm.

5.2.3 Numerical robustness of the multidirectional procedure: problem of the masonry shear panel

In Section 3.4, a smooth transition between different damage regions is proposed with the aim of alleviating the convergence difficulties expected when cracks close and re-open. In the present section, the effects of this procedure on the numerical performance of the multidirection damage approach are investigated and quantified with reference to the problem of the masonry shear panel studied in 5.2.1. This is carried out by varying the value of the parameter θ_t which identifies the amplitude of the transition region (see Eq. (32) and Fig. 7) for each level of permanent deformations considered in the numerical analyses (Fig. 24). The variable used to quantify the numerical performance is the number of iterations necessary to achieve convergence in a load step.

The convergence data which are discussed in the following regards the unloading-reloading stages after the achievement of the maximum load (cycle 2, amplitude 3 mm). As previously discussed, this is in fact the situation in which stiffness recovery is more emphasised and hence convergence difficulties are expected to be higher. Specifically, the load increments around crack-closure, which require the higher number of iterations to converge, are thirteen. For these thirteen load steps, the number of necessary iterations is indicated in Fig. 31.a, Fig. 31.b and Fig. 31.c, which refer to the case of high permanent deformations ($b^+ = 0.17$ and $b^- = 0.45$), intermediate permanent deformations ($b^+ = 0.1$ and $b^- = 0.3$) and null permanent deformations ($b^+ = 0.0$ and $b^- = 0.0$), respectively. In each graph, different values of θ_t are taken into account: from $\theta_t = \pi/180$ (1°) to $\theta_t = \pi/36$ (5°). Higher is θ_t, smoother is the modelling of the crak closure. Moreover, Fig. 31.d shows the structural responses obtained with different values of θ_t, in case of $b^+ = 0.1$ and $b^- = 0.3$.

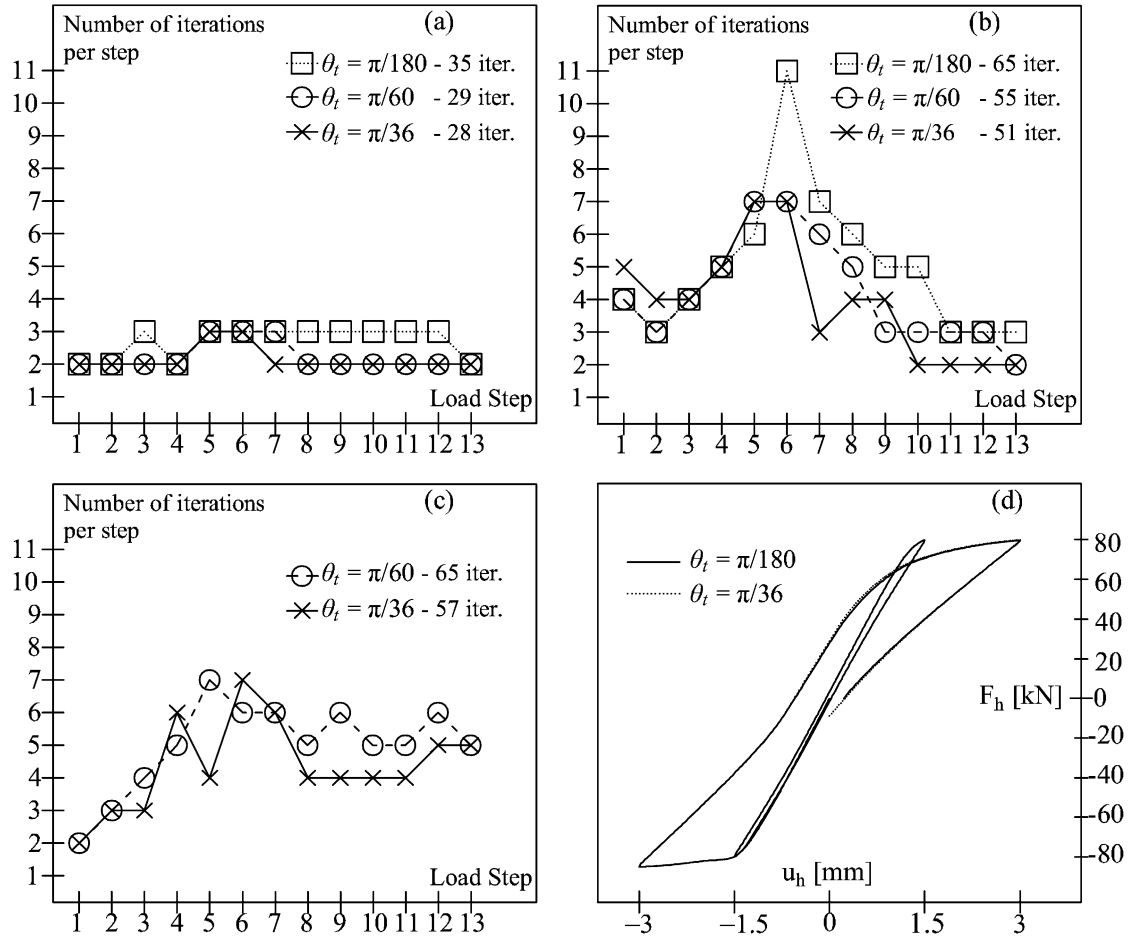

Figure 31 – Numerical convergence in correspondence of crack closure for varying θ_t: **(a)** high permanent deformations, **(b)** intermediate permanent deformations, **(c)** zero permanent deformations and **(d)** effects of θ_t on the structural response.

Analysing Fig. 31, it is possible to observe that, passing from $\theta_t = \pi/180$ to $\theta_t = \pi/36$, there is a non-negligible reduction of the total number of iterations, which is of 22% in the case of high $\boldsymbol{\varepsilon_p}$ and 24% in the case of intermediate $\boldsymbol{\varepsilon_p}$. However, the beneficial effect of the smoothing procedure is more significant in the case of zero permanent deformations, where the inclusion of a sufficiently wide transition region ($\theta_t = \pi/36$) allows to obtain convergence in 57 iterations, while, with the adoption of $\theta_t = \pi/180$, a lack of covergence has been encountered. For this reason the curve associated to $\theta_t = \pi/180$ is not present in Fig. 31.c. This consideration is in agreement with another trend inferable from Fig. 31: permanent deformations improve the numerical performance as they mitigate the abrupt stiffness changes in correspondence of crack closure. Finally, Fig. 31.d shows that the structural response is unaffected by the transition parameter θ_t, confirming that its role is only the one of improving the robusteness of the multidirectional damage procedure.

6. Conclusions

A d^+/d^- damage model based on the spectral decomposition of the reversible strain tensor, suitable for the analysis of quasi-brittle structures under monotonic and cyclic loadings, is presented.

The main aspects of the formulation are the following:

- The damage-induced orthotropy is modeled by means of the energy-equivalence assumption between nominal and effective configuration, with the consequent derivation of a constitutive operator (Eq. (4)) which is positive definite and symmetric.
- A multidirectional damage approach is adopted to deal with microcrack closure-reopening effects, especially effective in case of orthogonal, or however intersecting, set of cracks, typical of cyclic shear conditions (Section 3.1). The procedure consists in activating or deactivating a damage value on the base of the current principal strain directions, in order to simulate the opening and the closure of cracks, respectively. To improve the numerical robustness and performance, the modelling of these unilateral effects incorporates a smoothing procedure in the transition from an unloading stiffness to a reloading one.
- Permanent deformations $\boldsymbol{\varepsilon_p}$ are taken into account in a simplified as well as effective way and a modification (Eq. (25)) of the mesh-adjusted softening modulus proposed for linear and exponential softening is proposed with the aim of treating the evolution of the internal variables d^+, d^- and $\boldsymbol{\varepsilon_p}$ in a coupled way.
- The implementation of the constitutive model in a displacement-based finite element framework is ruled by a full strain-driven formalism.

The validation of the damage model is successfully carried out at a structural level, combining it with the crack band theory to ensure mesh size objective results.

Unreinforced concrete notched elements subjected to pure tension, pure bending and mixed-mode bending are considered to study the performance of the mechanical model under monotonic conditions. In addition, the same problems are analyzed with the damage model based on strain-equivalence, described in (Faria et al., 1998). No significant differences are appreciable in the structural responses obtained with the energy-equivalent model here proposed and the strain-equivalent one, being both of them able to fit adequately the experimental results. However, the adoption of the constitutive

symmetric operator $\boldsymbol{D_E}$ (Eq. (4)) is convenient in computational terms because it allows solving the algebraic system of equations with the Picard's method, referring to a symmetric secant stiffness matrix.

In order to validate the damage multidirectional approach, the problems of a masonry and a reinforced concrete panel subjected to in-plane cyclic shear are solved. In both the examples, the experimental evidence is satisfactorily reproduced in terms of lateral resistance, crack mechanisms, irreversible deformations, hysteretic behavior and symmetry in the response between loading and reloading. To highlight the enhanced stiffness recovery capabilities ensured by the new approach, a comparison between the results obtained with the multidirectional approach and with a pure scalar damage formulation is discussed. Moreover, by varying the intensity of the permanent strain tensor, the effect of this component on the structural response is also investigated, with the conclusion that a combined modelling of permanent deformations and unilateral effects is necessary in order to describe the real energy dissipation capacity of quasi-brittle structures under cyclic loading.

Finally, the adoption of permanent deformations is beneficial not only in terms of accuracy of the results but also in terms of numerical performance and robustness: the smoothing procedure introduced to alleviate convergence difficulties in presence of unilateral effects is more effective when irreversible strains are not considered.

Appendix A

The steps needed to derive the form of the exponential softening modulus $2H_d$ (25) are here shown. An adjusted expression for the softening modulus comes from the necessity of considering the evolution of the internal variables d^+, d^- and $\boldsymbol{\varepsilon_p}$ within a unified approach, treating in a combined way the two causes of dissipation, i.e. damage and irreversible deformations.

Referring to the expression for $\dot{\gamma}$ provided in Eq. (11), the energy per unit volume g_f dissipated in a monotonic loading history from an initial unstressed state to a complete damaged one can be evaluated through the following integral, as done in (Wu and Cervera, 2016):

$$g_f = \int_0^\infty \dot{\gamma} \cdot dt = -\int_0^\infty \left(\frac{\partial \psi}{\partial d^+} \cdot \dot{d}^+ + \frac{\partial \psi}{\partial d^-} \cdot \dot{d}^- \right) \cdot dt - \int_0^\infty \frac{\partial \psi}{\partial \boldsymbol{\varepsilon_p}} : \dot{\boldsymbol{\varepsilon}}_{\boldsymbol{p}} \cdot dt = g_{f\,d} + g_{f\,p} \qquad \text{(A.1)}$$

where the split between the specific fracture energy contribution due to damage (g_{fd}) and to permanent strains (g_{fp}) is put in evidence.

In order to express the relation between g_f and the softening modulus H_d, a 1D loading history is considered. Since analogous considerations can be found in 1D tension and in 1D compression, hereafter the superindex $^{\pm}$ is omitted. In a 1D stress-strain state, considering Eqs. (16), after the attainment of r_0 (Eq. (21)) the damage threshold r (Eq. (20)) can be expressed in terms of the reversible axial strain ε_e according to the relation:

$$r = E \cdot \varepsilon_e \qquad \text{(A.2)}$$

Since the damage energy release rates for the model here presented (Cervera and Tesei, 2017) coincide in the 1D case with the ones deriving from the model described in (Cervera, 2003), the first integral in Eq. (A.1) can be computed, considering the damage evolution laws (22), as follows:

$$g_{f\,d} = \int_{r_0}^{f_p} \frac{r^2}{2E} d'(r) \cdot dr + \int_{f_p}^{\infty} \frac{r^2}{2E} d'(r) \cdot dr = \frac{f^2}{E} \left(\bar{A}_d + \frac{1}{2H_d} + \frac{1}{2} \frac{f_p}{f} \right) \qquad \text{(A.3)}$$

where $\bar{A}_d = A_d \left(f_p^3 - 3 f_p \cdot f_e^2 + 2 \cdot f_e^3 \right) \Big/ \left(6 f \left(f_p - f_e \right)^2 \right)$.

For what concerns the computation of the dissipated energy due to irreversible deformations g_{fp}, the following relation holding in a 1D stress-strain state has to be considered:

$$\dot{\varepsilon}_p = \frac{b}{1-b}\dot{\varepsilon}_e \tag{A.4}$$

$$-\frac{\partial \psi}{\partial \varepsilon_p} = \sigma = \left(1-d\right)\cdot E \cdot \varepsilon_e \tag{A.5}$$

Therefore, taking into account Eqs. (A.4), (A.5) and the damage evolution laws (22), the second integral in Eq. (A.1) results:

$$\begin{aligned} g_{f\,p} &= \int_{r_0}^{f_p} \frac{b}{1-b}\frac{1}{E}\left(1-d(r)\right)\cdot r \cdot dr + \int_{f_p}^{\infty} \frac{b}{1-b}\frac{1}{E}\left(1-d(r)\right)\cdot r \cdot dr \\ &= \frac{b}{1-b}\frac{f^2}{E}\left(\tilde{A}_d + \frac{1}{2H_d}\right) \end{aligned} \tag{A.6}$$

where $\tilde{A}_d = \left(\frac{f_p^2}{2f^2} - \frac{{f_e}^2}{2f^2} - \frac{A_d\left(f_p - f_e\right)}{3f}\right)$.

Hence, collecting the expressions provided in Eqs. (A.3) and (A.6), the specific fracture energy (A.1) in a monotonic 1D loading history is the following:

$$g_f = \frac{f^2}{E}\left(\bar{A}_d + \frac{1}{2H_d} + \frac{1}{2}\frac{f_p}{f} + \frac{b}{1-b}\tilde{A}_d + \frac{b}{1-b}\frac{1}{2H_d}\right) \tag{A.7}$$

This quantity is equal, according to the crack band theory formulated in (Bažant and Oh, 1983), to the ratio between the fracture energy per unit surface G_f and the mesh length l_{dis}. Therefore, since G_f is a material property, the dissipation has to be maintained constant and this can be achieved by establishing a coupling between the dissipation related to damage g_{fd} and to permanent strains g_{fp}. According to this concept and specifically equating the fracture energy in the form (A.7) to the ratio G_f / l_{dis}, the expression for the softening modulus in Eq. (25) is derived. Note that for the limit case of $f_e = f = f_p$, the softening modulus in Eq. (25) reduces to:

$$2H_d = \frac{2}{\left(1-b\right)}\left(\frac{\bar{H}\cdot l_{dis}}{1-\bar{H}\cdot l_{dis}}\right) \tag{A.8}$$

where $\bar{H}$ is the material property defined as: $\bar{H} = f^2/\left(2E\cdot G_f\right)$. From Eq. (A.8), it is clear that higher is the parameter b, higher is the value of H_d. In addition, for $b = 0$, the softening modulus in (A.8) brings to a well-established result for linear and exponential softening (Cervera et al., 1996; Cervera, 2003).

On the contrary, computing the softening modulus as suggested in Eq. (26) means to neglect the dissipative contribution related to the permanent strains and to match only g_{fd} (Eq. (A.3)) to the ratio G_f / l_{dis}.

Four figures, Fig. A.1.a, Fig. A.1.b, Fig. A.2.a and Fig. A.2.b, show the differences between the unified dissipative approach here proposed (softening modulus (25)) and the uncoupled one (softening modulus (26)).

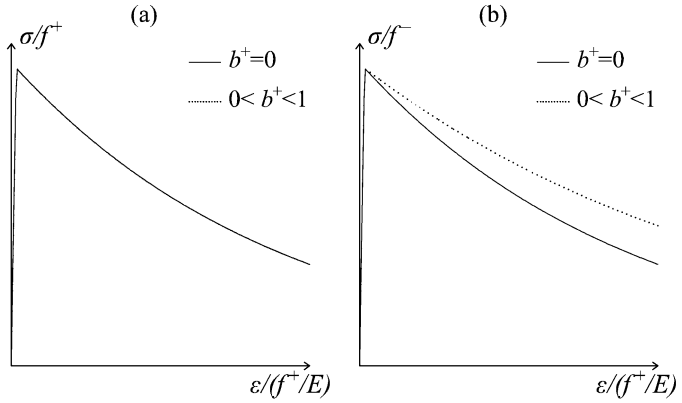

Figure A.1 – 1D tensile behavior: **(a)** unified dissipative approach for the computation of the internal variables (adoption of softening modulus (25)) and **(b)** uncoupled dissipative approach (adoption of softening modulus (26)).

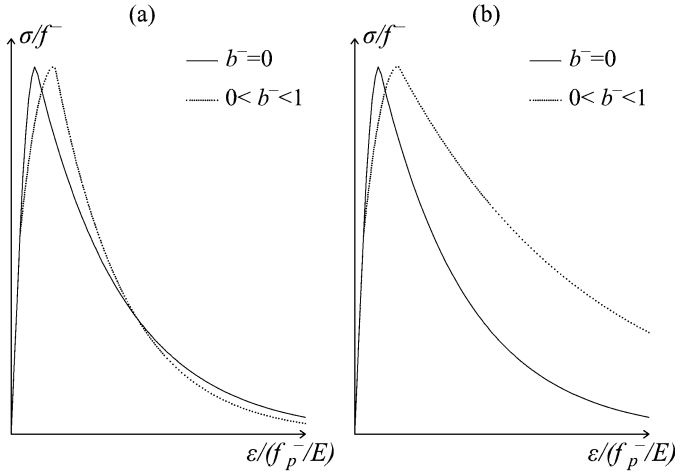

Figure A.2 – 1D compressive behavior: **(a)** unified dissipative approach for the computation of the internal variables (adoption of softening modulus (25)) and **(b)** uncoupled dissipative approach (adoption of softening modulus (26)).

In each figure, the 1D stress-strain curve in case of $b = 0$ (null irreversible deformations) and $0 < b < 1$ (non-null permanent deformations) are plotted. In Fig. A.1.a and Fig. A.1.b, the case of 1D tension in analysed while in Fig. A.2.a and Fig. A.2.b the case of 1D compression.

As evident from Fig. A.1.a and Fig. A.2.a, the energy released with or without permanent deformations is exactly the same resorting to the softening modulus (25), whereas a

relevant over-dissipation can be noticed with the adoption of the softening modulus (26) (Fig. A.1.b and Fig. A.2.b), passing from the case of $b = 0$ to the case of $0 < b < 1$.

References

Anthoine, A., Magonette, G., 1994. Shear-compression testing and analysis of brick masonry walls. Proc. 10th European Conference on Earthquake Eng. Vienna, 1657-1662.

Bažant, Z.P., 1983. "Comment on orthotropic models for concrete and geometarials", J. Eng. Mech. ASCE 109(3), 849-865.

Bažant, Z.P., Oh, B.H., 1983. Crack band theory for fracture of concrete. Mater. Struct. 16, 155-177.

Berto, L., Saetta, A., Scotta, R., Vitaliani, R. 2002. An orthotropic damage model for masonry structures. Int. J. Numer. Meth. Eng. 55, 127-157.

Bisch, Philippe, Erlicher, S., Huguet, M., 2014. Cracking in shear walls: experimental results and analytical predictions. Proc. 2nd European Conference on Earthquake Eng. Istanbul.

Contraffato, L., Cuomo, M., 2006. A framework of elastic–plastic damaging model for concrete under multiaxial stress states. Int. J. Plast. 22, 2272-2300.

Comi, C., Perego, U., 2001. Fracture energy based bi-dissipative damage model for concrete. Int. J. Solids Struct. 38, 6427-6454.

Caboche, J.L., 1992. Damage induced anisotropy: on the difficulties associated with the active/passive unilateral condition. Int. J. Damage Mech. 1(2), 148-171.

Carol, I., Rizzi, E., Willam, K, 2001. On the formulation of anisotropic elastic degradation. I. Theory based on a pseudo-logarithmic damage tensor rate. Int. J. Solids Struct. 38, 491-518.

Carol, I., Willam, K., 1996. Spurious Energy Dissipation/ Generation in Stiffness Recovery Models for Elastic Degradation and Damage. Int. J. Solids Struct. 33(20-22), 2939-2957.

Cervera, M., 2003. Viscoelasticity and Rate Dependent Continuum Damage Models. CIMNE Monograph n° 79, Barcelona, Spain.

Cervera, M.; Oliver, J.; Faria, R., 1995. Seismic evaluation of concrete dams via continuum damage models. Earthq. Eng. Struct. Dyn 24, 1225-1245.

Cervera, M., Oliver, J., Manzoli, O, 1996. A rate-dependent isotropic damage model for the seismic analysis of concrete dams. Earthq. Eng. Struct. D. 25(9), 987-1010.

Cervera, M. and Tesei, C., 2017. An energy-equivalent d^+/d^- damage model with enhanced microcrack closure-reopening capabilities for cohesive frictional materials. Materials 10(4), 433.

Chang, G.A., Mander, J.B., 1994. Seismic Energy Based Fatigue Damage Analysis of Bridge Columns: Part I – Evaluation of Seismic Capacity. Technical Report NCEER-94-0006, State University of New York at Buffalo.

Cicekli, U., Voyiadjis, G.Z., Abu Al-Rub, R.K., 2007. A plasticity and anisotropic damage model for plain concrete. Int. J. Plast. 23, 1874-1900.

Coleman, B.D., Gurtin, M.E., 1967. Thermodynamics with internal state variables. J. Chem. Phys. 47, 597-613.

Cope R.J., Rao, P.V., Clark, L.A., Norris, P., 1980. "Modelling of reinforced concrete behaviour for finite element analysis of bridge slabs", in Talor C. et al. (Eds.), Numerical method for nonlinear problems 1. Pineridge Press, Swansea, pp. 457-470.

Cordebois, J.P., Sidoroff, F., 1982. Endommagement anisotrope en elasticité et plasticité. J. Mec. Theor. Appl. Numéro Special, 45-60.

de Borst, R., 2002. Fracture in quasi-brittle materials: A review of continuum damage-based approaches. Eng. Fract. Mech. 69, 95-112.

de Borst, R., Nauta, P., 1985. Non-orthogonal cracks in a smeared finite element model. Eng Computations 2, 35-46.

Faria, R., Oliver, J., Cervera, M., 1998. A strain-based plastic viscous-damage model for massive concrete structures. Int. J. Solids Struct. 35(14), 1533-1558.

Faria, R., Oliver, J., Cervera, M., 2004. Modelling Material Failure in Concrete Structures under Cyclic Actions. J. Struct. Eng.-ASCE 130, 1997-2005.

Vecchio, F.J., 1999. Towards Cyclic Load Modeling of Reinforced Concrete. ACI Struct. J. 96(2), 193-202.

Gálvez, J.C., Elices, M, Guinea, G.V., Planas, J., 1998. Mixed mode fracture of concrete under proportional and non proportional loading. Int. J. Fract. 94, 267-284.

He, W., Wu, Y.F., Xu, Y., Fu, T.T., 2015. A thermodynamically consistent nonlocal damage model for concrete materials with unilateral effects. Comput. Methods Appl. Mech. Eng. 297, 371-391.

Horstemeyer, M.F., Bammann, D.J., 2010. Historical review of internal state variable theory for inelasticity. Int. J. Plast. 26, 1310-1334 .

Jefferson, A.D., Mihai, I.C., 2015. The simulation of crack opening-closing and aggregate interlock behavior in finite element concrete models. Int. J. Numer. Meth. Eng. 104, 48-78.

Ju, J.W., 1989. On energy-based coupled elastoplastic damage theories: Constitutive modelling and computational aspects. Int. J. Solids Struct. 25, 803-883.

Kormeling, H.A., Reinhardt, H.W., 1983. Determination of the fracture energy of normal concrete and epoxy modified concrete. In: Report 5–83-18, Delft University of Technology.

Krajcinovic, D., 2003. Damage Mechanics. Elsevier, B.V., Netherlands.

Lemaitre, J., Chaboche, J.L., 1978. Aspects phènomènologiques de la rupture par endommagement. J. Mec. Appl. 2, 317-365.

Lubliner, J., 1972. On the thermodynamics foundations of nonlinear solid mechanics. Int. J. Nonlinear Mech. 7, 237–254.

Lubliner, J., Oliver, J., Oller, S., Oňate, E., 1989. A plastic-damage model for concrete. Int. J. Solids Struct. 25(3), 299-326.

Magenes, G., Calvi, G.M:, 1992. Cyclic behavior of brick masonry walls. Proc. 10th World Conference on Earthquake Eng. Rotterdam, 3517-3522..

Magenes, G., Calvi, G.M:, 1997. In-plane seismic response of brick masonry walls. Earthq. Eng. Struct. D. 26, 1091-1112.

Mazars, J., Berthaud, Y., Ramtani, S., 1990. The unilateral behaviour of damaged concrete. Eng. Fract. Mech. 35, 629-635.

Menegotto, M., Pinto, P., 1973. "Method of analysis for cyclically loaded reinforced concrete plane frames including changes in geometry and non-elastic behavior of elements under combined normal force and bending." *Proc., IABSE Sympoium on Resistance and Ultimate Deformability of Structures Acted on by Well-Defined Repeated Loads*, Final Report, Lisbon.

Oliveira, D.V., 2003. Experimental and Numerical analysis of blocky masonry structures under cyclic loading. Ph.D. Thesis. Portugal: University of Minho.

Oliver, J., 1989. A consistent characteristic length for smeared cracking models. Int. J. Numer. Meth. Eng. 28(2), 461-474.

Ortiz, M., 1985. A constitutive theory for the inelastic behaviour of concrete. *Mech. Mater. 4*, 67-93.

Petracca, M., Pelà, L., Rossi, R., Oller, S., Camata, G., Spaccone, E., 2017 Multiscale computational first order homogenization of thick shells for the analysis of out-of-plane loaded masonry walls. Comput. Methods Appl. Mech. Eng. 315, 273-301.

Reinhardt, H., Cornelissen, H., 1984. Postpeak cyclic behaviour of concrete in uniaxial tensile and alternating tensile and compressive loading. Cem. Concr. Res. 14, 263-270.

Riggs, H.R., Powell, G.H., 1986. Rough crack model for analysis of concrete. J. Eng. Mech. ASCE 112 (5), 448-464.

Rospars, C., Chauvel, D., 2014. CEOS.fr ecperimental programme and reference speciement test results. Eur. J. Environ. Civ. Eng. 18 (7), 738-753.

Rots, J.G., Blaauwendraad, J., 1989. Crack models for concrete: discrete or smeared? Fixed, multidirectional or rotating? HERON 34(1), 1-59.

Rots, J.G., Nauta, P., Kusters, G.M.A., Blaauwendraad, J.,1985. Smeared crack approach and fracture localization in concrete. HERON 30(1), 1-48.

Saloustros, S., Pelà, L., Cervera, M., Roca, P., 2017. Finite Element Modelling of Internal and Multiple Localized Cracks. Computat. Mech. 59 (2), 299-316.

Simo, J.C., Ju, J.W., 1987. Strain- and stress-based continuum damage models-I. Formulation. Int. J. Solids Struct. 23, 821-840.

Toti, J., Marfia, S., Sacco, E., 2013.Coupled body interface nonlocal damage model for FRP detachment. Comput. Methods Appl. Mech. Eng. 260, 1-23.

Trunk,B., 2000. Einfluss der Bauteilgroesse auf die Bruchenergie von Beton. Aedificatio Publishers, (in German).

Vassaux, M., Richard, B., Ragueneau, B., Millard, A., 2015. Regularised crack behaviour effects on continuum modelling of quasi-brittle materials under cyclic loading. Eng. Fract. Mech. 149, 18-36.

Vecchio, F.J., Collins, M.P., 1986. The modified compression-field theory for reinforced concrete elements subjected to shear. J. Am. Concrete Inst. 83 (2), 219-231.

Voyiadjis, G.Z., Taqieddin, Z.N., Kattan, P.I., 2008. Anisotropic damage-plasticity model for concrete. Int. J. Plast. 24, 1946-1965.

Wu, J.Y., Cervera, M., 2016. A thermodynamically consistent plastic-damage framework for localized failure in quasi-brittle solids: Material model and strain localization analysis. Int. J. Solids Struct. 88-89, 227-247.

Wu, J.Y, Li, J., 2008. On the mathematical and thermodynamical descriptions of strain-equivalence based anistropic damage model. Mech. Mater. 40, 377-400.

Wu, J.Y., Li, J., Faria, R., 2006. An energy rate-based plastic-damage model for concrete. Int. J. Solids Struct. 43, 583-612.

Wu, J.Y, Xu, S.L., 2013. Reconsideration on the elastic damage/degradation theory for the modelling of microcrack closure-reopening (MCR) effects. Int. J. Solids Struct, 50,795-805.

Xue, X., Yang, X., 2014. A damage model for concrete under cyclic actions. Int. J. Damage Mech. 23(2), 155-177.

Yazdani, S., Schreyer, H.L., 1990. Combined plasticity and damage mechanics model for plain concrete. J. Eng. Mech. ASCE 116, 1435-1450.